



# Tortuosity Determination of Battery Electrodes and Separators by Impedance Spectroscopy

Johannes Landesfeind,<sup>a,\*</sup> Johannes Hattendorff,<sup>a,\*</sup> Andreas Ehrl,<sup>b</sup> Wolfgang A. Wall,<sup>b</sup> and Hubert A. Gasteiger<sup>a,\*\*</sup>

<sup>a</sup>Chair of Technical Electrochemistry, Department of Chemistry and Catalysis Research Center, Technische Universität München, Munich, Germany

<sup>b</sup>Institute for Computational Mechanics, Department of Mechanical Engineering, Technische Universität München, Munich, Germany

Lithium ion battery performance at high charge/discharge rates is largely determined by the ionic resistivity of an electrode and separator which are filled with electrolyte. Key to understand and to model ohmic losses in porous battery components is porosity as well as tortuosity. In the first part, we use impedance spectroscopy measurements in a new experimental setup to obtain the tortuosities and MacMullin numbers of some commonly used separators, demonstrating experimental errors of <8%. In the second part, we present impedance measurements of electrodes in symmetric cells using a blocking electrode configuration, which is obtained by using a non-intercalating electrolyte. The effective ionic resistivity of the electrode can be fit with a transmission-line model, allowing us to quantify the porosity dependent MacMullin numbers and tortuosities of electrodes with different active materials and different conductive carbon content. Best agreement between the transmission-line model and the impedance data is found when constant-phase elements rather than simple capacitors are used.

© The Author(s) 2016. Published by ECS. This is an open access article distributed under the terms of the Creative Commons Attribution Non-Commercial No Derivatives 4.0 License (CC BY-NC-ND, <http://creativecommons.org/licenses/by-nc-nd/4.0/>), which permits non-commercial reuse, distribution, and reproduction in any medium, provided the original work is not changed in any way and is properly cited. For permission for commercial reuse, please email: [oa@electrochem.org](mailto:oa@electrochem.org). [DOI: 10.1149/2.1141607jes] All rights reserved.

Manuscript submitted March 3, 2016; revised manuscript received April 8, 2016. Published April 28, 2016.

**Motivation.**—Advanced battery models are a valuable tool for evaluating the performance, safety, and life-time of lithium ion batteries, since they can provide insight into the kinetics and the transport characteristics of batteries, which are not or only partially accessible by experiments. To obtain quantitative and meaningful numerical results, the choice of appropriate physical models and boundary conditions with the corresponding, accurately determined, kinetic and transport parameters are key issues. For numerical simulations of battery systems, the ion-transport model for concentrated electrolyte solutions introduced by Newman et al.<sup>1</sup> is frequently used. Since the microscopic geometry of actually used porous electrodes and separators are largely unknown, a homogenization approach is applied for the macroscopic description of porous media. In this case, the influence of the microstructure on the macroscopic behavior is modeled by additional geometric parameters such as the porosity  $\epsilon$  and the tortuosity  $\tau$ . The porosity  $\epsilon$  is a well-defined property of a porous medium, which can be determined easily. In contrast, the effective tortuosity of separators and particularly of electrodes are more difficult to quantify, and, to further complicate the matter, many different definitions for the tortuosity  $\tau$  are used in the literature. Thus, the different tortuosity definitions will be presented prior to reviewing the literature concerned with determining the tortuosity or the effective ionic conductivity of porous battery separators and electrodes.

**Definitions of Tortuosity and MacMullin Number.**—In the following, the most common definitions describing the influence of the microstructure on the macroscopic behavior are introduced. As explained in, e.g., Patel et al.,<sup>2</sup> the effect of a porous microstructure on the macroscopic conservation laws can be described by the MacMullin number  $N_M$

$$N_M = \frac{\kappa}{\kappa_{\text{eff}}} \quad [1]$$

which relates the ionic conductivity  $\kappa$  of the electrolyte solution to the effective ionic conductivity  $\kappa_{\text{eff}}$  of a porous separator or electrode. The MacMullin number is the basis for many empirical laws established

to describe the influence of the porous microstructure of separators and electrodes on the macroscopic conservation laws in terms of the porosity  $\epsilon$  and additional parameters. One of the most famous empirical laws was introduced by Archie<sup>3</sup>

$$N_M = \epsilon^{-m} \quad [2]$$

where a power-law relationship between the porosity  $\epsilon$  of sandstone and the MacMullin number  $N_M$  with the exponent  $m$  (Archie's exponent) is used. Other empirical laws are given, e.g., in the review by Shen and Chen<sup>4</sup> or in Barrande et al.<sup>5</sup> As mentioned before, these empirical laws hold "only for a series of samples from the same geological formation, because these rocks have similar microstructures".<sup>6</sup> For a different type of microstructure, the exponential factor  $m$  may be quite different. The MacMullin number as well as the related empirical laws are based on a macroscopic view of the porous medium.

In contrast, it is also possible to use a microscopic approach to model a porous microstructure. In this case, the tortuosity is introduced as a measure of the elongation of the transport path due to the porous structure with respect to a straight line  $d$ . For example, the path-length tortuosity

$$\tau_{\text{path}} = \frac{d_{\text{path}}}{d} \quad [3]$$

is defined for a single channel with a constant cross-sectional area. The tortuosity can also be defined with respect to a physically motivated length definition. For instance, the path length of the electronic tortuosity  $\tau_{\text{el}}$  is based on the gradient of the potential. Last but not least, the geometrical tortuosity  $\tau_{\text{geo}}$  is defined as the shortest connection between two points  $x_1$  and  $y_1$  with respect to the length of the straight connection between these points. The path-length tortuosity  $\tau_{\text{path}}$ , the geometrical tortuosity  $\tau_{\text{geo}}$ , and the physically motivated tortuosity  $\tau_{\text{el}}$  are not identical and may result in different numerical values. Until a few years ago, all microscopically motivated values for the tortuosity were usually based on simplified geometries such as channel networks or regular porous structures such as agglomerated spheres (see, e.g., Wyllie and Rose,<sup>7</sup> Cornell and Katz<sup>8</sup> or Zalc et al.<sup>9</sup>). More recently, realistic three-dimensional representations of complex porous structures can be provided by imaging technologies, enabling a numerical quantification of the mean geometrical tortuosity  $\bar{\tau}_{\text{geo}}$ ,<sup>10</sup> which is based on an averaged value of the shortest path lengths  $d_{ij}$

\*Electrochemical Society Student Member.

\*\*Electrochemical Society Fellow.

<sup>z</sup>E-mail: [j.landesfeind@tum.de](mailto:j.landesfeind@tum.de)

between points  $x_i$  and  $y_j$  and is usually determined by numerical algorithms utilizing the random walk theory<sup>11</sup> or the graph theory.<sup>10</sup> Note that these numerical algorithms only consider the elongation of the transport path but do not include additional factors such as non-constant cross-sectional areas or the microscopic surface structure of the solids constituting the porous medium. Therefore, the constriction factor  $\beta$  is sometimes introduced to account for a non-constant cross-sectional area. The concept of the constriction factor and its theoretical motivation is, e.g., explained by Wiedenmann et al.,<sup>10</sup> using the following relation

$$N_M \equiv \frac{\tau_{\text{geo}}}{\varepsilon\beta} \quad [4]$$

The big advantage of the microscopic approach is that it is based on a purely geometrical description of the microstructure, so that a basic understanding for a porous structure is generated which can be used for the design of future porous materials. However, the size of the reconstructed sample has to be considered as potential source of uncertainty, since it has to be large enough to be representative as, e.g., can be observed in Cooper et al.<sup>12</sup>

In the above discussion, macroscopic and microscopic approaches for the determination of tortuosity parameters were reviewed. In addition, it is also possible to simply apply the microscopic concept of tortuosity to the macroscopic description of a porous medium using an empirical approach

$$N_M = \frac{\tau}{\varepsilon} \quad [5]$$

in which the effective tortuosity  $\tau$  is determined experimentally for each given porous medium. In this case, the effective tortuosity  $\tau$  does not only describe the elongation of the transport path, but also includes other effects such as variable cross-sectional areas, surface morphologies, etc. As emphasized by Holzer et al.,<sup>6</sup> it is important to strictly distinguish between the effective tortuosity  $\tau$  and the geometrical tortuosity  $\tau_{\text{geo}}$ , since they are based on different definitions. The main advantage of the former is that all geometrical effects are automatically included in the effective tortuosity  $\tau$ . However, its main disadvantage is that it is only accessible experimentally and therefore might include experimental artifacts and also does not allow to project values for other geometries (e.g., particle shapes, porosities, etc.). At this point, it is important to mention that the tortuosity  $\tau$  in Eq. 5 appears often as  $\tau^2$ , which is the result of different assumptions as, e.g., discussed in Clennell<sup>13</sup> or Djian et al.<sup>14</sup> The same macroscopic concept can be applied to reconstructed, three-dimensional microstructures. In this case, the MacMullin number in Eq. 5 is not determined by experiments but by numerical simulation of the Laplace equation as discussed, e.g., in Ender et al.,<sup>35</sup> Joos et al.<sup>15</sup> and Cooper et al.<sup>12</sup> A similar concept is used in Ebner and Wood,<sup>16</sup> in which the effective tortuosity is computed numerically from top and cross sectional views of electrodes based on either NMC ( $\text{Li}(\text{Ni}_x\text{Mn}_y\text{Co}_z)\text{O}_2$ ;  $x + y + z = 1$ ), LCO ( $\text{LiCoO}_2$ ), or graphite. As for determination of the geometrical tortuosity based on reconstructed microstructures, the sample size has to be considered as a potential uncertainty.

The last important definition which is frequently used in battery applications results from the combination of Eqs. 2 and 5

$$\tau = \varepsilon^{1-m} = \varepsilon^{-\alpha} \quad [6]$$

This well-known equation with the exponent  $\alpha$  is frequently called the Bruggeman relation<sup>17</sup> although the origin of this convention is unclear (see note added in proof). Unfortunately, in some cases the tortuosity is also defined differently, e.g., as  $\tau = \varepsilon^{(1-\alpha)}$ .<sup>18</sup> The Bruggeman exponent relates to Archie's exponent by  $-\alpha = 1 - m$ . For spherical particles the Bruggeman exponents becomes  $\alpha = 0.5$  (as defined in Eq. 6), corresponding to an Archie's exponent  $m = 1.5$ . This simplest case of the Bruggeman equation for spherical particles is used for comparison in the Results and discussion section. This case corresponds to the so-called Bruggeman approximation frequently used for porous electrodes as suggested in Newman and Thomas-Alyea<sup>1</sup> and implemented in commercial software packages

(e.g., Comsol Multiphysics), where it is expressed terms of  $\varepsilon/\tau = \varepsilon^{1.5}$ . The validity of this relation was investigated experimentally as well as numerically, and reasonably close agreement was reported in the case of spherically shaped solids forming the porous medium.<sup>2,19,20</sup> For more complex structures, different  $\alpha$ -values are obtained, whereby frequently Eq. 6 is modified by an additional proportionality factor  $f$ .<sup>18,19</sup>

$$\tau = f \varepsilon^{-\alpha} \quad [7]$$

In this work, we will examine the validity of the Bruggeman equation for spherical particles ( $\tau = \varepsilon^{-0.5}$ , i.e.  $\alpha = 0.5$ ) by comparing it with tortuosities determined for separators and porous electrodes. The functional description of the tortuosity is analyzed by fitting experimental data for a variety of separators and electrodes with the general equation for the tortuosity used in literature (Eq. 7).

**Literature Overview.—Ionic Conductivity in Separators.**—In the literature, different values for the MacMullin number  $N_M$ , the coefficient  $\alpha$ , or the tortuosity  $\tau$  of various separators can be found.<sup>2,14,22</sup> In many publications, impedance based techniques are used to measure the effective conductivity. Unfortunately, the value of the MacMullin numbers vary quite significantly for the same separator material which, e.g., can be illustrated for the reported MacMullin numbers for Celgard 2500 separator of 8.5 (Patel et al.<sup>2</sup>), 13 (Djian et al.<sup>14</sup>) and of 18 (Abraham<sup>22</sup>). Quite clearly, this large scatter suggests the presence of experimental artifacts in at least some of the measurements, which still needs to be resolved. Gas transport resistance measurements are also commonly used to characterize separators, whereby the so-called Gurley number (the time in seconds it takes for 100 cm<sup>3</sup> of air to pass through a defined area at a defined pressure difference) is often assumed to be proportional to the effective ionic resistivity.<sup>23</sup> While useful for a rough benchmarking of separators, Gurley numbers cannot be quantitatively related to the effective ionic resistance.

**Ionic Conductivity in Electrodes.**—For electrodes, the determination of the MacMullin number is more elaborate, since now the porous medium is electronically conductive, so that the high-frequency resistance cannot be used as a measure of the ionic conductivity. The effective ionic conductivity of electrodes can in principle be determined by AC impedance using a transmission-line model (TLM).<sup>24</sup> This, for example, was used to quantify the proton conductivity of PEM (proton exchange membrane) fuel cell electrodes by Liu et al.,<sup>25</sup> where the charge transfer resistance in the TLM circuit model could be eliminated experimentally by removing the reacting gases. The resulting TLM circuit model is often referred to as being under *blocking conditions*. For lithium ion batteries, Ogihara et al. measured electrodes in a symmetric cell setup with a lithium salt electrolyte,<sup>26,27</sup> showing that they would obtain blocking conditions by conducting the impedance analysis at a state of charge (SOC) of 0% or 100%, where lithium intercalation/deintercalation is suppressed. Using the simplified TLM circuit model for blocking conditions, they could obtain effective ionic resistances of the electrodes from a fit.

An alternative method was used by Thorat et al.<sup>18</sup> and Holzer et al.,<sup>6</sup> who determined the MacMullin number of porous electrodes by the ratio of the effective binary diffusion coefficient in the electrode and the binary diffusion coefficient in the pure electrolyte. Here, polarization interrupt experiments allow the determination of the effective binary diffusion coefficient for a freestanding electrode sheet (prepared by delamination of the electrode from the current collector) placed between two separators by comparison with numerical simulations.<sup>18,28</sup> However, the two drawbacks of this method are that freestanding electrodes have to be prepared and that the numerical model requires knowledge of the concentration-dependent values of the transference number, the thermodynamic factor, and the diffusion coefficient. A more recently developed method by DuBeshter et al.<sup>29</sup> is based on measuring the pressure-dependent term of the gas diffusion coefficient through a porous electrode, which, however, is only valid

for isotropic electrode morphologies, i.e., if the in-plane permeability is equal to the through-plane permeability. This clearly is not satisfied for flake- or plate-like particles characteristic for many graphites.

Finally, the effective ionic conductivity can in principle also be determined numerically if the exact morphology and microstructure can be determined.<sup>30,31</sup> 3D reconstructions of porous electrodes can be obtained using X-Ray tomography<sup>32,33</sup> or focused ion beam scanning electron microscopy (FIB-SEM).<sup>34</sup> The tortuosity  $\tau$  of many types of active materials, with a defined 3D-structure obtained from advanced imaging technologies, is often determined by numerical simulations as shown, e.g., for  $\text{LiFePO}_4$ <sup>12,35</sup> or for  $\text{La}_{0.58}\text{Sr}_{0.4}\text{Co}_{0.2}\text{Fe}_{0.8}\text{O}_{3-\delta}$  (LSCF) cathodes.<sup>15</sup> For a reconstructed graphite electrode, the geometrical tortuosity  $\tau_{\text{geo}}$  determined by the random walk theory was found to be consistent with the tortuosity  $\tau$  determined by a physically motivated simulation.<sup>11</sup> Numerical investigations of 3D reconstructed electrodes based on X-Ray tomography data have shown the effect of particle anisotropy on the through-plane tortuosity, reporting increasing tortuosities when the particle shape is changed from spherical and non-spherical to platelet like graphite particles.<sup>32</sup> The limited spatial resolution of current 3D-imaging methods is still somewhat of a drawback, since detailed imaging of conductive carbons (primary particle diameters of  $\approx 0.04 \mu\text{m}$  and primary particle agglomerates of  $\approx 0.4 \mu\text{m}$ ) would be required to include the effect of conductive carbon additives on the effective ionic conductivity of electrodes. This drawback can be mitigated by a combination of X-Ray tomography data with carbon binder modelling.<sup>33</sup>

The present work aims at quantifying the tortuosity of porous separators and electrodes used in lithium ion batteries using electrochemical impedance spectroscopy measurements. A new test setup will be shown to quickly and reproducibly determine the effective ionic conductivity of separators. To quantify the effective ionic conductivity of electrodes, a more general transmission-line model compared to that used by Ogihara et al.<sup>26,27</sup> will be used with symmetric electrodes, whereby measurement requirements to avoid experimental artifacts will be examined. To investigate whether the effective tortuosity of electrodes can be described by the power-law relationship of the Bruggeman equation and how it will vary across different electrodes, we will examine a number of electrodes composed of different electrode active materials at different compositions and compressions. Comparison of particle sizes, morphologies, and the electrode compositions are investigated toward their impact on the MacMullin number.

## Theory

**Ion transport through porous structures.**—Charge transport in porous particle networks or structures such as lithium ion battery electrodes or separators is determined by the ionic resistance  $R_{\text{ion}}$  inside the electrolyte phase. If the ionic resistance  $R_{\text{ion}}$  through a cross-sectional area  $A$  of a material with porosity  $\epsilon$  and a thickness  $d$  can be determined, and if the conductivity of the electrolyte  $\kappa$  is known, the MacMullin number  $N_M$  and the tortuosity  $\tau$  can be calculated by rearranging Ohm's law using Eqs. 1 and 5

$$N_M = \frac{\tau}{\epsilon} = \frac{R_{\text{ion}} \cdot A \cdot \kappa}{d} \quad [8]$$

Note that the determination of the MacMullin number does not require knowledge of the electrode porosity, while it is required to determine the tortuosity. Techniques to measure ionic resistances  $R_{\text{ion}}$  will be discussed in the next paragraphs for both separators and electrodes. For impedance based approaches, so-called *blocking electrodes* or *blocking conditions* are frequently used, which means that there is no charge transfer across the solid/liquid interface, i.e., that the surface is ideally polarizable.<sup>36</sup> Such conditions can be realized experimentally, if no charge transfer reaction can take place in the potential window under investigation. Implementation of blocking conditions may be realized by using a salt which cannot react electrochemically with the electrodes within the potential excitation of a few mV during an impedance measurement. In reality, surface roughness<sup>37</sup> or an inhomogeneous current distribution<sup>38</sup> may alter the ideally polarizable

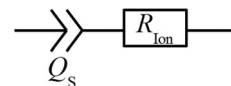


**Figure 1.** Equivalent circuit for non-electronically conducting porous separators in a blocking electrode configuration.

behavior of electrodes, and a blocking electrode is therefore generally described best by a constant-phase Element (CPE), the complex impedance of which is given as

$$Z_{\text{CPE}} = \frac{1}{Q(i\omega)^\gamma} \quad [9]$$

where  $\omega$  is the angular frequency, the parameter  $Q$  is related to the electrode capacitance, and  $\gamma$  is the constant phase exponent (for  $\gamma = 1$ ,  $Z_{\text{CPE}}$  simplifies to the impedance of an ideal capacitor).

**Ionic resistance of a separator.**—Impedance measurements of electrolyte-filled electronically insulating separators, positioned between two electrodes in a blocking electrode condition can be described by an equivalent circuit consisting of a serial connection of two CPEs and an ionic resistance, whereby the CPEs can be lumped into one global CPE as depicted in Figure 1.

The impedance of the equivalent circuit in Figure 1 is given by

$$Z_{\text{Sep.}} = R_{\text{ion}} + \frac{1}{Q_S(i\omega)^\gamma} \quad [10]$$

which allows for a simple determination of the ionic resistance  $R_{\text{ion}}$  inside the porous separator by means of a high frequency extrapolation ( $\omega \rightarrow \infty$ ) in the corresponding Nyquist plot.

**Ionic resistance of a porous electrode.**—The impedance of electrolyte filled pores in an electronically conductive particle network, such as in a lithium ion battery electrode, can be described by an equivalent circuit model referred to a transmission-line model (TLM).<sup>36</sup> Figure 2 depicts the equivalent circuit of the general TLM. Inside the solid phase, the electronic resistance is represented by a serial connection of ohmic resistors,  $r_{\text{el}}$ . Accordingly, the ionic resistances in the electrolyte phase are depicted by the ohmic resistors  $r_{\text{ion}}$ . In addition, charge can be transferred between the solid and the liquid phase via faradaic or capacitive charge transfer reactions, which is described by the surface impedance elements  $z_s$ .

This equivalent circuit segment may then be connected ionically and/or electronically on either/or both ends. For example, for an electrode coated on a current collector and pressed against a separator, the electronic rail (upper brown rail in Figure 2) is connected only at one end and the ionic rail (lower blue rail in Figure 2) is connected only at the other end, as no ions can flow into the current collector (pure electron conductor) and now electrons can flow into the electrolyte (pure ion conductor). For practical purposes, the use of a separator is advantageous in order to prevent an electronic short-circuit between the two electrodes and to keep the electrodes in a plane-parallel configuration. For properly designed lithium ion battery

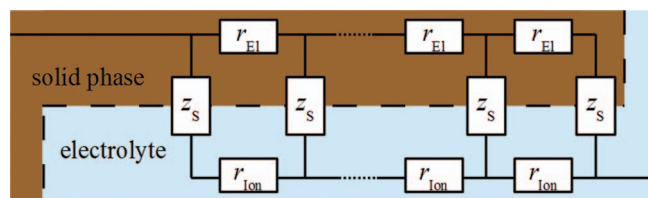


**Figure 2.** Equivalent circuit of the general transmission-line model for a porous electrode. The charge transfer process between the solid and the liquid phase through faradaic or capacitive charge transfer reactions is represented by  $z_s$ . Electrons are moving in the solid phase (brown region), while ions are moving in the electrolyte phase (blue region).



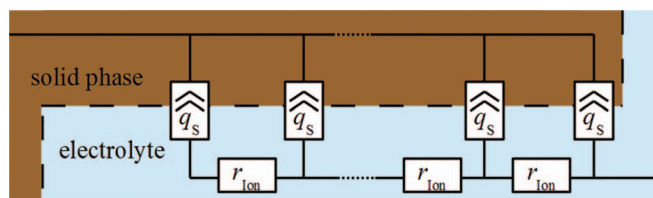


**Figure 3.** Simplified form of the transmission-line model for porous electrodes with  $r_{EI} \ll r_{ion}$  and for blocking conditions.

electrodes, the electronic resistance in the solid phase  $r_{EI}$  of the transmission-line model is negligibly small ( $\kappa > 0.1$  S/cm) due to the presence of conductive carbon additives<sup>39,40</sup> compared to the resistance in the electrolyte phase  $r_{ion}$  ( $\kappa < 0.01$  S/cm). This means that the electronic resistances  $r_{EI}$  are generally negligible compared to the ionic resistances  $r_{ion}$ , so that the former can usually be omitted. Further simplifications can be made for blocking conditions, i.e., in the absence of faradaic charge transfer reactions, in which case the surface impedance elements  $z_s$  can be modeled by a capacitive behavior. The latter is modeled using constant-phase elements to account for geometric effects resulting from the materials surface roughness.<sup>41</sup> For lithium ion batteries, blocking conditions were shown to be approached at 0% and 100% SOC;<sup>26,27</sup> as we will show later, they can also be realized by using non-intercalating electrolyte salts, which are stable within the potential window of an impedance measurement ( $\pm 10$  mV). Thus, lithium ion electrodes in a blocking condition and with  $r_{EI} \ll r_{ion}$ , the general transmission-line model reduces to a form depicted in Figure 3.

An analytical electrode impedance  $Z_{EL}$  can be derived for the simplified transmission-line model<sup>36,42</sup> in Figure 3, which we will refer to as TLM-Q:

$$Z_{EL} = \sqrt{R_{ion} Z_s} \coth \left( \sqrt{\frac{R_{ion}}{Z_s}} \right) = \sqrt{\frac{R_{ion}}{Q_s(i\omega)^\gamma}} \coth \left( \sqrt{Q_s(i\omega)^\gamma R_{ion}} \right) \quad [11]$$

where  $R_{ion} = \Sigma(r_{ion})$  and  $Q_s = \Sigma(q_s)$ . If an ideal capacitive behavior would be assumed instead of the constant-phase elements, the constant-phase exponent  $\gamma$  becomes one and the  $1/(Q_s(i\omega)^\gamma)$  terms reduce to the impedance of a capacitor  $1/(i\omega C)$ . The transmission-line model with pure capacitive behavior of the surface impedance elements will be referred to as TLM-C. Exemplary Nyquist plots of the porous electrode transmission-line models with constant-phase exponents of  $\gamma = 1$  (pure capacitor) and  $\gamma = 0.9$  are shown in Figure 4 together with a 45° slope as a guide for the eye.

The Nyquist plot in Figure 4 shows that the TLM-C model (solid line) results in a vertical line toward low frequencies, while the TLM-Q model (dashed line) deviates toward lower angles from a vertical line at low frequencies. In addition, at high frequencies, the TLM-C model shows a 45° slope, while the TLM-Q model displays a slope with an angle smaller than 45°. One way to extract the electrode ionic resistance  $R_{ion}$  of electrodes via impedance measurements is to fit Eq. 11 to experimental data. Exemplary fits are shown in the Results and discussion section. The ionic resistance can also be obtained via linear extrapolations of the low and high frequency regions to the x-axis in the Nyquist plots. While the latter extrapolation gives the high frequency resistance  $R_{HFR}$ , the extrapolation of the low frequency branch to the x-axis ( $Z_{EL}|_{(\omega_{low} \rightarrow \infty)}$ ) gives the sum of the high frequency resistance and one third of the ionic resistance inside the pores, as already discussed by Ogihara et al.<sup>26</sup> or Liu et al.<sup>25</sup> for the transmission-line model with ideal capacitors:

$$Z_{EL}|_{(\omega_{low} \rightarrow \infty)} = \frac{R_{ion}}{3} + R_{HFR} \quad [12]$$

Similarly, it can be shown, that if constant-phase elements instead of ideal capacitors are used in the transmission-line model, the same relation holds.

## Experimental

**Materials and electrodes.**—Separators from Celgard (Celgard 3500, Celgard H2013, Celgard C480, Celgard 2320, Celgard 2500, Celgard 2325), Separion (S240P30), two commercial single-layer HDPE separators (#1 and #2) and Freudenberg (FS-3001-30) were punched to circular discs of at least 25 mm diameter and dried in a vacuum oven at 70°C overnight. Composite electrodes were prepared by doctor-blade coating of a slurry of active material (AM), binder (Kynar HSV 900, Arkema), conductive carbon (SuperC65, Timcal), and NMP (Sigma Aldrich, anhydrous, 99.5%) prepared in a planetary mixer (Thinky ARV-310), using a copper current collector foil (MTI, 19  $\mu$ m) for anode active materials and an aluminum current collector foil (MTI, 15  $\mu$ m) for cathode active materials. Coatings were dried in a self-built drying oven at 50°C under air and then punched to circular discs of 11 mm diameter. Compression to the desired electrode porosity was done in a hydraulic press (Mauthe, PE-011). Further drying was done in a vacuum drying oven at a minimum temperature of 95°C for at least 6 h. Commercially available active materials, electrode compositions, and the abbreviation by which the electrode will be referred to further on are listed in Table 1.

Electrodes were characterized by measuring their weight (Mettler Toledo, XP6, 1  $\mu$ g accuracy) and thickness (Mitutoyo, Lifematic, VL-50, 0.1  $\mu$ m accuracy). These were used to calculate the electrode porosity, assuming the bulk active material densities listed in Table 1 as well as the bulk density of the conductive carbon of  $\sim 2.2$  g/cm<sup>3</sup>. The absolute error in the thickness measurements is ca.  $\pm 2$   $\mu$ m (corresponding to ca. 4–10% for coating thicknesses ranging from 20–50  $\mu$ m) and the absolute error in the weight measurements is estimated to be  $\pm 0.01$  mg/cm<sup>2</sup>. The resulting error in electrode porosity is represented by horizontal error bars in Figure 15, Figure 19 and Figure 20.

An argon filled and temperature controlled glove box (MBraun, 25°C  $\pm$  1°C, oxygen and water content <0.1 ppm, Ar 5.0, Westfalen, 99.999%vol.) was used for electrolyte preparation, the measurement of the effective ionic resistance of separators, and for cell assembly. All cell parts were cleaned thoroughly by boiling them in an ethanol water mixture, rinsing them with water (Millipore, Elix, 15 M $\Omega$ ), and then drying them at 70°C in a drying oven before bringing them into the glove box. Mixtures of ethylene carbonate (EC, Sigma Aldrich, anhydrous, 99%), diethyl carbonate (DEC, Sigma Aldrich, anhydrous, >99%), and dimethyl carbonate (DMC, Sigma Aldrich, anhydrous,  $\geq 99\%$ ) were used as solvents for self-prepared electrolytes containing tetrabutylammonium perchlorate (TBAClO<sub>4</sub>, Sigma Aldrich,  $\geq 99.0\%$ ) salt. Impedance measurements of separators were

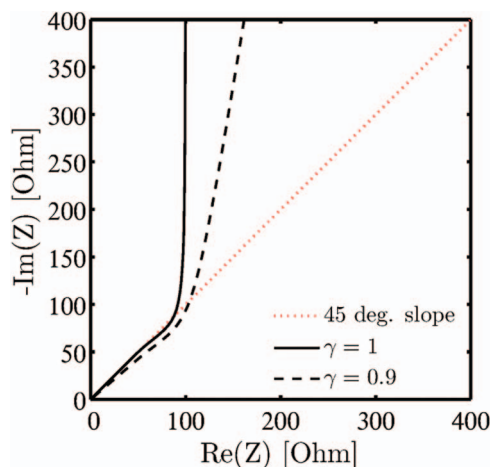


**Figure 4.** Simulated Nyquist plots of Eq. 11 with  $R_{ion} = 300 \Omega$ ,  $Q = 100 \mu F \cdot s^{\gamma-1}$ , and  $\gamma = 1$  (solid) or  $\gamma = 0.9$  (dashed); the dotted red line indicates a 45° slope.

**Table I.** Electrodes prepared for the determination of the MacMullin number and the tortuosity by the TLM-Q model. LFP, LNMO, and NMC were coated on aluminum current collectors, while LTO and graphite were coated on copper current collectors. Listed active material loadings are the mean loadings ( $\pm 10\%$ ) of the electrodes shown in Figure 15.

Active Material (AM)	Loading	Density (AM)	%wt AM/binder/carbon	Referred to as
LFP (commercial)	8 mg <sub>AM</sub> /cm <sup>2</sup>	3.6 g/cm <sup>3</sup>	90/5/5	LFP-lowC
LFP (commercial)	3 mg <sub>AM</sub> /cm <sup>2</sup>	3.6 g/cm <sup>3</sup>	70/15/15	LFP-highC
LNMO (commercial)	7 mg <sub>AM</sub> /cm <sup>2</sup>	4.5 g/cm <sup>3</sup>	96/2/2	LNMO
NMC 111 (commercial)	18 mg <sub>AM</sub> /cm <sup>2</sup>	4.7 g/cm <sup>3</sup>	96/2/2	NMC
LTO (commercial)	9 mg <sub>AM</sub> /cm <sup>2</sup>	3.5 g/cm <sup>3</sup>	90/5/5	LTO
graphite (SGL Carbon GmbH)	6 mg <sub>AM</sub> /cm <sup>2</sup>	2.3 g/cm <sup>3</sup>	95/5/0	graphite-1
graphite (KS6L, Timcal)	4 mg <sub>AM</sub> /cm <sup>2</sup>	2.3 g/cm <sup>3</sup>	91/9/0	graphite-2

conducted using commercially available LP572 electrolyte from BASF (EC:EMC (3:7 w:w) with 1 M LiPF<sub>6</sub> + 2% VC).

**Measurement cells.**—Three cell setups were used for the determination of the MacMullin number and the tortuosity of porous separators and electrodes. A turn-key conductivity sensor (LF 1100+, SI Analytics, with custom made ground glass fitting) with a built-in temperature sensor was used to measure the conductivity of the used electrolytes at 25°C.

First, the impedance of separators filled with electrolyte was measured inside a glove box in an open setup consisting of two cylindrical copper blocks, which were connected with actively shielded cables to a potentiostat outside the glove box. A schematic sketch of the copper block setup is shown in Figure 5.

An excess of electrolyte in the open copper block setup allows for good wetting and exact measurement of the ionic resistance as long as the measurement time does not exceed a few minutes, even if small amounts of solvent evaporate. In order to precisely confine the effective area, it is necessary to insulate the perimeter of the upper copper electrode. This was done with epoxy resin (EPO5.S200, Composite Technology), polished to a sharp edge with a polishing machine (Beta Grinder-Polisher, Buehler).

Second, symmetrical Swagelok type T-Cells (spring-compressed to  $\approx 1$  bar) were used to measure the impedance of porous electrodes (11 mm diameter) via the transmission-line model. Cells were assembled inside the glove box and then transferred into a temperature controlled climate chamber (25°C, Binder). In such a symmetrical setup, the measured impedance corresponds to the sum of the impedances of the individual electrodes. Therefore, care was taken to always combine two electrodes with closely matched loading and porosity. Two glass fiber separators (VWR, thickness 250  $\mu$ m, borosilicate, binder-free, 1.2  $\mu$ m pore size) with a diameter of 11 mm were used as separators.

Third, pouch bag cells were used, which consisted of a stack of a large electrode, a larger separator and a smaller counter electrode as schematically depicted in Figure 6. An uncoated/inactive part of the copper foil was led outside the pouch bag and used as a current collector tab. For measurements of the separator resistance, two copper foils were used as electrodes. Determination of the ionic resistance of porous electrodes in the pouch cell setup was done by placing

a glass fiber separator between the electrodes under investigation. Precise determination of the active area in pouch cells was achieved by image analysis. Typical dimensions were 20  $\times$  20 mm<sup>2</sup> for the larger electrode, 30  $\times$  40 mm<sup>2</sup> for the separator and 15  $\times$  15 mm<sup>2</sup> for the smaller electrode. The cells were filled with  $\approx 50$ –200  $\mu$ l electrolyte, depending on the size and the type of separator, and then vacuum sealed at 25 mbar. Four point electronic connections to the potentiostat (Biologic VMP3 potentiostat/galvanostat) were used to avoid contact resistances.

Electrochemical impedance spectra were measured around OCV. A frequency range of 200 kHz to 1 kHz with a 5 mV perturbation was used for determining ionic resistances of separators, and from 200 kHz to 0.5 Hz with a 10 mV perturbation for measurements of the transmission-line ionic resistance of electrodes.

## Results and Discussion

**Determination of separator tortuosities and macmullin numbers.**—Ohmic resistances of porous lithium ion battery separators were determined with impedance measurements using the copper cell described in the Experimental section (Figure 5). In this setup, stray currents are avoided by electrical insulation around the upper copper electrode. The necessity of this insulation is demonstrated with Figure 7, where impedance spectra of 1, 2, or 3 separator layers were measured in the copper block setup with and without the insulation around the upper copper electrode. Measurements for each number of separator layers are repeated three times with fresh separators and a freshly cleaned cell. In total, this results in nine measurements with the insulated and nine measurements with the non-insulated upper copper electrode. Although shown for different separators and electrolytes, leading to different high frequency resistances, the very same trend would exist for a direct comparison of the same separator.

Figure 7a shows a large variation of the impedance spectra if the non-insulated upper copper electrode is used; note that repeated impedance spectra for any given assembled cell are reproducible, suggesting that the variability is not due to noise in the impedance measurements. This experimental scatter can be eliminated by electronically insulating the perimeter of the upper copper electrode as

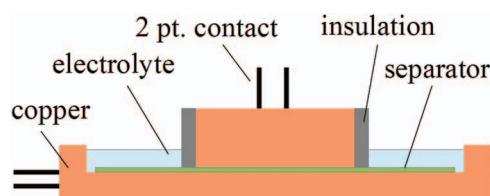


**Figure 5.** Sketch of copper block setup for the determination of the ionic resistance of electrolyte-filled separators. The upper copper electrode has a height of 10 mm and a diameter of 20 mm; the lower copper electrode has a height of 15 mm, a diameter of 50 mm, and the electrolyte reservoir has a depth of 5 mm (typically filled to a height of  $\approx 2$  mm) and an inner diameter of 45 mm; the diameter of the sandwiched separator is  $\geq 25$  mm.

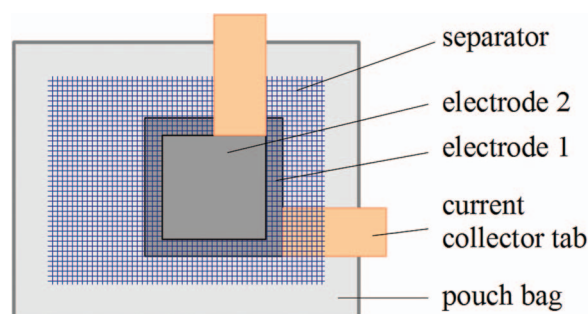


**Figure 6.** Schematic of pouch bag cell setup for symmetrical impedance measurements of transmission-line model of porous electrodes.

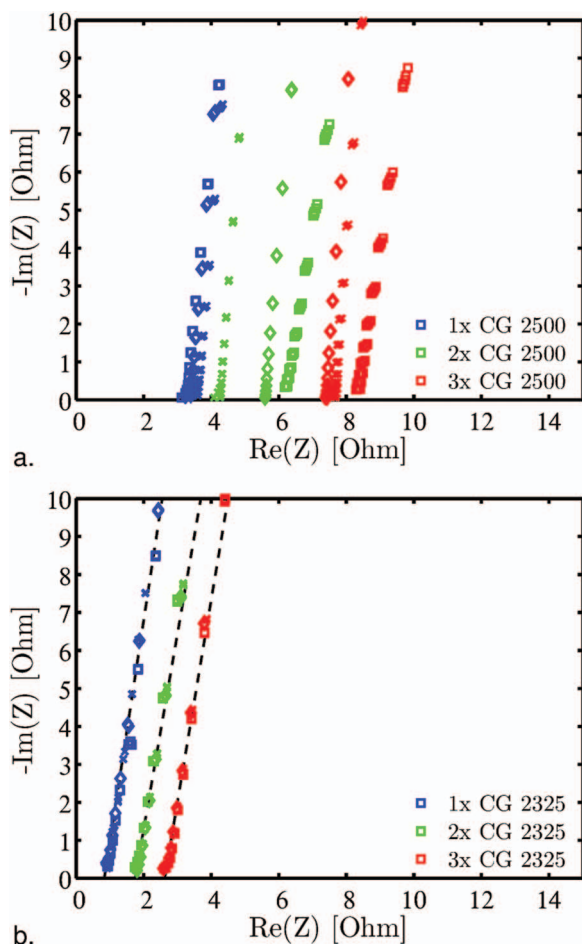


**Figure 7.** High frequency resistance of multiple layers of Celgard 2325 (with 1 M LiPF<sub>6</sub> in EC:EMC (3:7 w:w) + 2% VC) or Celgard 2500 (with 0.05 M LiPF<sub>6</sub> in EC:DEC (1:1 w:w) separators, in copper block setup with a. non-insulated upper electrode and b. an insulated upper electrode to avoid stray fields and currents. Three independent repeat experiments (crosses, squares, diamonds) are shown for each experimental configuration (one, two and three separators, highlighted by colors).

shown in Figure 7b, where three independent repeat experiments (crosses, squares, diamonds) for each separator stacking yield identical impedance spectra (the remaining very small variations can be seen by regarding the rightmost red squares at the lowest frequencies). We conclude that the experimental scatter observed with the non-insulated upper copper block electrode (Figure 7a) is not due to unstable impedance measurements, but is caused by stray currents that bypass through the electrolyte and effectively increase the probed separator area by an unknown extent. By insulating the perimeter of the upper copper electrode, this effect can be eliminated, resulting in highly reproducible measurements (Figure 7b). Owing to in-plane ionic conduction in the separator, the effective separator diameter is larger than the upper copper electrode diameter (20 mm) by an effective length which is on the order of three separator thicknesses. Assuming a maximum separator thickness of  $\approx 75 \mu\text{m}$  (stacking of three separators), this would correspond to an effectively sampled area of  $\approx 3.28 \text{ cm}^2$  vs. the nominal sample area of  $3.14 \text{ cm}^2$ , which would introduce a maximum error in the determined areal resistance and effective conductivity of less than 5%.

Before application of this simple experimental setup to various battery separators, the accuracy of this new device will be verified by varying the separator thickness using multiple separator layers, by changing the electrolyte conductivity, and by comparing results obtained in pouch cells (see Figure 6) and in the copper block setup (see

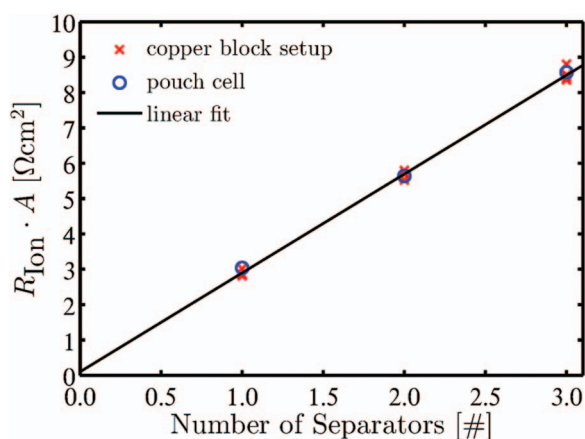


**Figure 8.** High frequency areal resistance of multiple layers of Celgard 2325 separators soaked with 1 M LiPF<sub>6</sub> in EC:EMC (3:7 w:w) + 2% VC using both the copper block setup (four repeat experiments per stacking) and pouch cells (one experiment per stacking). The line represents a least-squares fit of all the data to  $R_{\text{Ion}} \cdot A = x_1 \cdot \#_{\text{Sep}} + x_0$ , yielding  $x_0 = 0.10 \Omega \text{ cm}^2$  and  $R^2 = 0.998$ .

Figure 5). At first, the areal resistances of multiple layers of Celgard 2325 separators obtained from measurements with both the copper block setup and in pouch cells are compared and depicted in Figure 8.

Results from both pouch cells (blue circles in Figure 8) and from the copper block setup (red crosses in Figure 8) are in excellent agreement. The standard deviations for each separator count of measurements conducted in the copper block setup are below 3.5%, which is on the order of the assumed separator porosity and thickness variances. Furthermore, Figure 8 shows the expected perfectly linear relationship between areal resistance and the number of separators. The negligibly small y-intercept of  $x_0 = 0.1 \Omega \text{ cm}^2$  of the least-squares regression line in Figure 8 demonstrates that no significant additional resistive contributions (e.g., from contact resistances) are present in either setup (i.e.,  $x_0$  is  $<3\%$  of the overall resistance of a separator). Figure 8 also serves as a quality measure with regards to experimental artifacts which could arise from incomplete separator wetting. For different numbers of separators and in completely different cell setups, in which electrolyte is added either at ambient pressure (copper block setup) or the cell is sealed at an absolute pressure of 25 mbar (pouch bag setup), no difference in areal resistance could be observed.

In order to further verify the measurement setup, we also examined whether the measured tortuosity for a given separator is independent of electrolyte conductivity, as one would expect. Tortuosities were calculated for single layers of Celgard 2325 based on impedance measurements in the copper block setup and using porosity and thickness values specified by the manufacturer (see Table II). Data with five different electrolytes are compared in Figure 9, including the experimental data obtained with the copper block setup already shown in Figure 8 (data set at  $\sim 9.5 \text{ mS/cm}$ ; light-blue symbols).

Independent of solvent, salt, or salt concentration, a tortuosity of  $4.03 \pm 0.24$  is obtained from measured high frequency resistances as depicted in Figure 9. Compared to the standard deviation of  $\sim 3\%$  obtained from variation of the number of separators or the cell setup in Figure 8, an increased standard deviation of  $\sim 6\%$  is obtained from these experiments with different electrolytes. Part of this error is due to temperature fluctuations caused by the glovebox's temperature control ( $\pm 1.0^\circ\text{C}$ ). In addition, very low electrolyte conductivities for electrolytes with small salt concentrations (left-hand side data set in Figure 9) are prone to errors from impurities, while high electrolyte conductivities (right-hand side data set in Figure 9) lead to small ionic resistances in which case signal contributions from cable inductivities and small contact resistances are more significant. Therefore, the best measurement conditions were found for electrolyte conductivities in the range of 3–10 mS/cm, with separator samples cut to a diameter of 25 mm or 40 mm. Such electrolytes are also closest to relevant



**Table II.** Tortuosities ( $\tau$ ) and MacMullin numbers ( $N_M$ ) of porous separators determined by impedance measurements in blocking electrode configuration using the setups shown in Figure 5 and Figure 6, mainly using individual separator layers and 1 M LiPF<sub>6</sub> in EC:EMC (3:7 w:w) + 2% VC electrolyte ( $\kappa = 9.25$  mS/cm). The listed separator porosity ( $\epsilon$ ) and thickness ( $d$ ) values were taken from the manufacturers' specification sheets (separator parameters differing from the manufacturers' specification sheet are marked by an asterisk) and used in Eq. 8 to calculate  $\tau$  and  $N_M$  values. The MacMullin number predicted by the Bruggemann relationship for spherical particles ( $N_{M(B)} = \epsilon^{-1-\alpha}$ ) based on Eqs. 5 and 6 with  $\alpha = 0.5$  and values from the literature ( $N_{M(lit.)}$ ) are shown in the right-hand-most columns. Variations in  $\tau$  and  $N_M$  indicate the standard deviations based on at least three independent repeat experiments.

Separator	Type	$\epsilon$ [-]	$d$ [ $\mu$ m]	$\tau$ (meas.)	$N_M$ (meas.)	$N_{M(B)}$	$N_{M(lit.)}$
commercial (#1)	monolayer HDPE	0.39	18.5	$5.4 \pm 0.4$	$14 \pm 1.1$	4.1	
commercial (#2)	monolayer HDPE	0.43	16	$6.9 \pm 0.1$	$16 \pm 0.3$	3.6	
Celgard H2013	trilayer	0.47	20	$3.2 \pm 0.2$	$6.9 \pm 0.5$	3.1	
Celgard 2320	trilayer	0.39	20	$3.9 \pm 0.0$	$10 \pm 0.1$	4.1	$6.5^{*23}, 11^{*44}$
Celgard 2325	trilayer	0.39	25	$4.1 \pm 0.2$	$10 \pm 0.6$	4.1	$7.0^{*23}$
Celgard 2500	monolayer PP	0.55	25	$2.5 \pm 0.2$	$4.5 \pm 0.3$	2.5	$13^{*14}, 8.5^{*2}, 18^{*22}$
Celgard 3500	coated PP	0.55	25	$3.4 \pm 0.1$	$6.1 \pm 0.2$	2.5	
Celgard C480	trilayer	0.50	21.5	$3.6 \pm 0.3$	$7.3 \pm 0.5$	2.8	
Freudenberg FS-3001-30	non-woven PET	0.60	28	$2.7 \pm 0.0$	$4.6 \pm 0.1$	2.2	$14^{43}$
Separion S240P30	non-woven PET	0.46	28.1	$4.3 \pm 0.2$	$8.6 \pm 0.3$	2.8	

electrolytes for lithium ion batteries. The predicted tortuosity of  $\tau = 1.6$  for the Celgard 2325 separator based on the Bruggeman estimation for spherical particles (i.e.,  $\tau = \epsilon^{-0.5}$  obtained from Eq. 6 with  $\alpha = 0.5$ ) and a porosity of  $\epsilon = 0.39$  (see lower dashed blue line in Figure 9) is only 40% of the experimentally obtained value, illustrating that the simple Bruggeman estimate for spherical particles but frequently applied to separator materials can lead to large errors. That this indeed seems to be the case for essentially all commonly used separators will be shown in the following.

Averaged results from impedance measurements on various separators in both setups (pouch cell and copper block setup) are summarized in Table II, listing porosity ( $\epsilon$ ) and thickness ( $d$ ) values taken from the manufacturers' specification sheets, whereby our own thickness measurements were in excellent agreement with the specified values. Tortuosities ( $\tau$ ) and MacMullin numbers ( $N_M$ ) were obtained from the measured ionic resistance ( $R_{ion}$ ) values and the specified separator properties using Eq. 8. While separator porosity and thickness values are needed to calculate  $\tau$ , calculation of  $N_M$  only requires the easily measureable separator thickness, so that the latter will allow for a more straightforward comparison with the literature. For this reason, Table II also lists the literature values for the MacMullin number

( $N_{M(lit.)}$ ) of various separators in addition to the MacMullin number predicted by the Bruggeman equation for spherical particles ( $N_{M(B)}$ ), obtained by combining Equations 5 and 6 ( $N_{M(B)} = \epsilon^{-1-\alpha}$ ) and using  $\alpha = 0.5$ . The standard deviations of the calculated tortuosities and MacMullin numbers in Table II are below 8% for each separator type, which suggests reasonably good reproducibility of the measurements. As already suggested above, the discrepancies between experimentally determined MacMullin numbers ( $N_M$ ) and theoretical estimates based on the Bruggeman equation ( $N_{M(B)}$ ) are substantial in all cases, consistent with previous literature reports.<sup>2,18,21</sup> Even the smallest discrepancy between  $N_M$  and  $N_{M(B)}$ , determined for the Celgard 2500 separator, amounts to a factor of  $\sim 1.8$ , which in the most extreme cases increases to a factor of  $\sim 4.5$  (see Table II).

A comparison of the here determined values of  $N_M$  with the literature ( $N_{M(B)}$ ) shows significant deviations. For example, based on the effective resistance values of Celgard 2320 and Celgard 2325 trilayer separators, the data reported by Arora and Zhang<sup>23</sup> correspond to  $N_M$  values of  $\sim 6.5$  and  $\sim 7.0$ , which are substantially lower than our values of  $10 \pm 0.1$  and  $10 \pm 0.6$ , respectively (see Table II). Likewise, a similarly large discrepancy is found when comparing the MacMullin numbers of  $13 \pm 1.5$ ,<sup>14</sup>  $8.5$ ,<sup>2</sup> and  $18$ <sup>22</sup> reported for Celgard 2500, in contrast to the value of  $4.5 \pm 0.3$  obtained in our measurements. Finally, the product specification sheet<sup>43</sup> for the Freudenberg FS-3001-30 separator lists an ohmic resistivity which would correspond to a threefold larger  $N_M$  value compared to our measurements (second to last row in Table II). To a lesser degree, these discrepancies in MacMullin number may be due to variations in the separator microstructure, e.g., caused by modifications during production. An indication for different separator microstructures is the difference in reported separator thickness and porosity values by Djian et al.<sup>14</sup> for Celgard 2500 (23  $\mu$ m and 0.47 respectively) compared to our Celgard product specification sheet, which lists values of 25  $\mu$ m and 0.55 respectively. We believe, however, that the majority of these discrepancies are due to a combination of several effects: i) stray currents caused by the geometry of the conductivity measurement setup (e.g., an ionic bypass through the electrolyte between the cell wall and the separator could have led to the systematically lower MacMullin values reported by Arora and Zhang<sup>23</sup>); ii) substantial contact resistances in coin cell based two-point probe measurements (e.g., Patel et al.<sup>2</sup> subtracted a contact resistance of 0.35  $\Omega$ , while the expected separator resistance based on our results is of the same order of magnitude, viz., 0.57  $\Omega$ ); iii) artifacts caused by the stacking of a large number of separators, often used to minimize contact resistance effects and/or to probe the effect of separator compression (e.g., Cannarella and Arnold<sup>44</sup> determined the separator resistance by stacking 32 separators, which for anisotropic materials may differ from measurements on a single separator); and/or, iv) uncertainties in

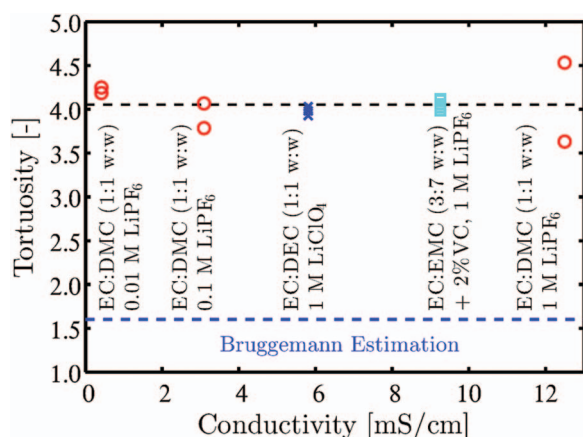


**Figure 9.** Tortuosities of a Celgard 2325 separator based on high frequency resistance measurements (copper block setup) versus electrolyte conductivity, spanning a range of 0.41 to 12.5 mS/cm (the specific electrolytes are listed in the figure). Tortuosities are based on a porosity of  $\epsilon = 0.39$  and a thickness of  $d = 25$   $\mu$ m as specified by the manufacturer, and are calculated using Eq. 8. The blue dashed line indicates the  $\tau$ -value based on the Bruggemann estimation for spherical particles (Eq. 6, with  $\alpha = 0.5$ ).

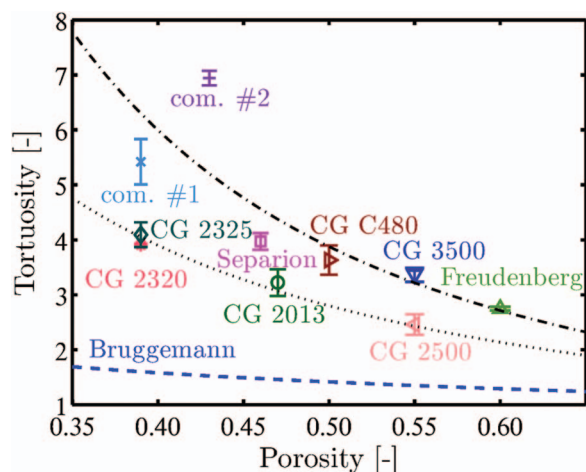


**Figure 10.** Tortuosities of porous separators (Celgard is abbreviated with CG) and their standard deviations determined via high frequency resistance measurements (data from Table II). Fits with Eq. 6 using  $\alpha = 2.5$  (dotted line, i.e.,  $\tau = \varepsilon^{-2.5}$ ) and  $\alpha = 3.1$  (dashed-dotted line, i.e.,  $\tau = \varepsilon^{-3.1}$ ) vs. the conventionally used Bruggeman coefficient for spherical particles of  $\alpha = 0.5$  (blue dashed line).

the effective geometric area of the separator probed in conventional conductivity-cells (likely the cause in the data reported by Abraham<sup>22</sup>). Although the MacMullin numbers reported in the literature scatter substantially, we believe that our here presented measurement setups and procedures provide a precise and reliable methods for determination of separator ionic resistances. While pouch cell measurements were used as a consistency check for our copper block setup, we believe that the copper block setup allows for equally precise results at reduced experimental effort (e.g., no vacuum sealing device is needed and experiments can be repeated quickly).

As seen above for a large variety of available separators, the Bruggeman equation (Eq. 6) with  $\alpha = 0.5$  (i.e.,  $\tau = \varepsilon^{-0.5}$ ) is not valid for typical lithium ion battery separators (see  $N_M$  vs.  $N_{M(B)}$  in Table II). Thus, we will compare obtained separator tortuosities with the generalized Bruggeman equation (Eq. 6 with free  $\alpha$ ). Figure 10 depicts the separator tortuosities and their standard deviations listed in Table II as a function of porosity as well as two fits to Eq. 6 ( $\alpha = 2.5$  and  $\alpha = 3.1$ ) and a plot of the conventional Bruggeman equation for spherical particles with  $\alpha = 0.5$ .

The tortuosities of the separators Celgard H2013, Celgard 2320, Celgard 2325 and Celgard 2500 are well reproduced by  $\tau = \varepsilon^{-2.5}$  ( $\alpha = 2.5$ ), while the separators from Freudenberg, Separion, the commercial single-layer HDPE separators (#1 and #2) and the separators Celgard C480 and Celgard 3500 fit reasonably well to  $\tau = \varepsilon^{-3.1}$  ( $\alpha = 3.1$ ). An indication for the difference between these groups of separators may be gained by comparing Celgard 2500 and Celgard 3500. According to the manufacturer's specification sheet, these separators have identical materials properties (thickness, gurley number, porosity, pore size, TD and MD shrinkage, puncture strength, as well as TD and MD tensile strength),<sup>45</sup> and the only specified difference is that Celgard 3500 is surfactant-coated. For further identification of the differences between the two separator groups which can be discerned in Figure 10, more details on the preparation process, the detailed separator morphology and the presence and types of surfactant coatings would be necessary.

As a conclusion, from impedance measurements using the insulated copper block setup, precise tortuosity values and MacMullin numbers could be obtained for a wide variety of commonly used separators, with standard deviations of  $<8\%$ . In all cases, the Bruggeman estimation for spherical particles (Eq. 6, with  $\alpha = 0.5$ ), which is frequently used in battery models, largely underestimates the real ionic resistances through the porous separators.

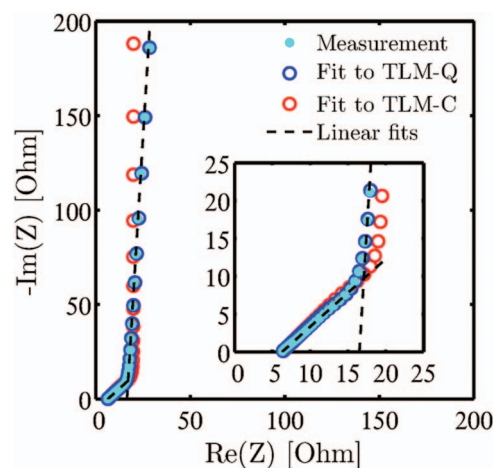


**Figure 11.** Exemplary impedance spectrum (200 kHz to 0.5 Hz) of two electrodes (graphite-1 (Table I) with thickness of 63.2  $\mu\text{m}$ , porosity of 0.41, and effective area of 2.37  $\text{cm}^2$ ) assembled in a symmetrical pouch cell with one Celgard 2325 separator using 50 mM TBAClO<sub>4</sub> in EC:DMC (1:1 w:w) with a bulk conductivity of 1.74 mS/cm (light blue solid circles). The data are fitted to either the TLM-C model (red open circles) or the TLM-Q model (blue open circles); linear extrapolations to the high and low frequency branches of the TLM-Q model are indicated by the dashed lines. The inset is a magnified view of the high frequency range.

**Determination of electrode tortuosities and MacMullin numbers.—Differentiation to literature.**—Prior to discussing our impedance measurements with porous electrodes, the methodology suggested in this work is compared with the work of Ogihara et al.<sup>26</sup> The differences between the two approaches are in the details of the used equivalent circuit model and in the realization of a blocking electrode configuration. While Ogihara et al.<sup>26</sup> used a transition-line model with pure capacitors to describe the surface impedance at the pore walls (TLM-C model, i.e.,  $\gamma = 1$  in Eq. 11), a constant-phase element is used in this work (TLM-Q model, i.e.,  $\gamma \neq 1$  in Eq. 11). The latter leads to a  $<90^\circ$  slope in the low frequency branch of the Nyquist plot, as already shown for simulated Nyquist plots in Figure 4. To illustrate the influence of a constant-phase element versus a perfect capacitor, graphite electrodes (graphite-1, see Table I) were prepared as outlined in the Experimental section and assembled in symmetrical cells. An exemplary impedance spectrum of such a cell is shown in Figure 11.

The impedance spectrum in Figure 11 shows a TLM behavior starting at a high frequency resistance of  $R_{\text{HFR}} = 6.35 \Omega$ , a value which corresponds to the ohmic resistance of the separator and which is consistent with the data shown in Table I (for the electrode area and electrolyte used in Figure 11, a resistance of 6.1  $\Omega$  would be predicted for the used Celgard 2325 separator). Figure 11 shows an excellent agreement between the experimental data (light blue solid circles) and the TLM-Q model fit according to Eq. 11 (blue open circles). According to Eq. 12, the difference between the x-axis values obtained from the linear extrapolations of the low and the high frequency branches of the TLM-Q model (dashed lines) corresponds to one third of the ionic resistance of both electrodes. From Figure 11, the thus determined ionic resistance for both electrodes equates to 31.6  $\Omega$ , which is in excellent agreement with the value of 31.0  $\Omega$  resulting from a fit of the experimental data to the TLM-Q model equation (Eq. 11). On the other hand, a more than 30% larger ionic resistance for both electrodes of 40.6  $\Omega$  is found when the same dataset is fitted to the TLM-C model as suggested by Ogihara et al.,<sup>26</sup> whereby this discrepancy is a result of the mismatch between the TLM-C model fit and the experimental data at low frequencies (see Figure 11). It should be emphasized that the experimental data neither in our work (see Figure 11) nor in the work by Ogihara et al.<sup>26</sup> (see Figure 6 of Ref. 26) show a perfectly vertical low frequency branch, so that the



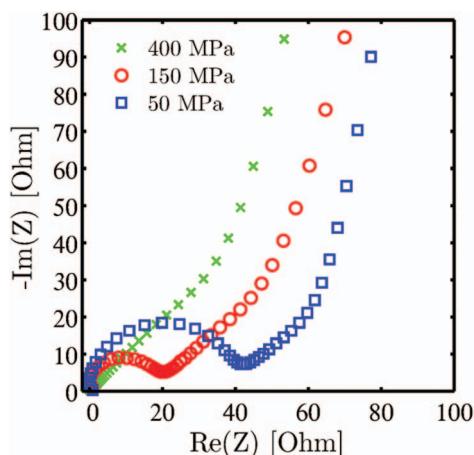


**Figure 12.** Exemplary Nyquist plots, subtracted by the HFR for better comparability, of LFP electrodes with low conductive carbon content (LFP-highC electrodes, see Table I) after different compressions: 50 MPa, 150 MPa, and 400 MPa, yielding porosities of 0.49, 0.34, and 0.27. The frequency maxima of the semi-circles are  $f_{\max}(50 \text{ MPa}) \approx 4 \text{ kHz}$  and  $f_{\max}(150 \text{ MPa}) \approx 10 \text{ kHz}$ . Measured in symmetrical T-cells with one glass fiber separator using 10 mM TBAClO<sub>4</sub> in EC:DMC (1:1 w:w) with a bulk conductivity of 0.46 mS/cm.

accuracy of the TLM-C model will largely depend on the selected low-frequency cutoff in the fitting procedure. For this reason, the TLM-Q model used in our work is preferred, as its fitting results are substantially less sensitive to the chosen low frequency cutoff value.

In addition to the different transmission-line circuit used by Ogihara et al.,<sup>26</sup> these authors also used a lithium ion containing electrolyte for their symmetrical cell measurements. In this case, blocking conditions were assumed to hold for freshly prepared electrodes at 0% and 100% state-of-charge (SOC), supported in their measurements by the absence of a semi-circle in the Nyquist plot, which would be expected if lithium intercalation/deintercalation were to occur. However, in our preliminary experiments with lithium ion containing electrolytes (not shown), semi-circles were observed for some of the electrodes listed in Table I, even at 0% and 100% SOC. As will be discussed below, this may be due to either an insufficiently suppressed charge-transfer reaction and/or electronic contact resistances. Since the use of a non-intercalating electrolyte (TBAClO<sub>4</sub>) allows for an explicit assignment of an observed semi-circle feature to electronic contact resistances between coating and current collector, non-intercalating electrolytes were used in our work.

**Current collector – coating contact resistances.**—Prior to investigating the impact of active material particle size/morphology and electrode composition on the electrode's ionic resistance, impedance spectra of LFP cathodes will be analyzed after different compression steps. It will be shown that any compression-dependent contact resistances between current collector and electrode coating can be determined from an analysis of the impedance spectra obtained with a non-intercalating electrolyte.

Electrodes for lithium ion batteries are usually compressed or calendered to reduce their porosity, thereby enhancing the volumetric energy density while at the same time increasing the electronic conductivity across the electrode coating and across the current collector/coating interface. High carbon content LFP electrodes (LFP-highC, see Table I) were compressed to different porosities and assembled in symmetrical T-Cells, separated by two glass fiber separators. A high carbon content was chosen to ensure a high electronic conductivity within the coating in order to satisfy the assumption of negligible electronic resistances between the particles within the coating, which was made in the theoretical part of this work (see Figure 3).

Figure 12 shows the impedance spectra recorded of LFP-highC electrodes coated on an aluminum current collector and compressed by 50 MPa, 150 MPa and 400 MPa before assembly, shifted to the ori-

gin of the complex plane for better comparability. Although medium and low frequencies show the expected TLM for all compressions, a prominent difference can be observed at high frequencies. A distinct  $R/Q$  element dominates the high frequency region at a compression of 50 MPa, with the resistance of the high frequency semi-circle amounting to  $\sim 40 \Omega$ . Similar electrodes compressed at a three-fold higher pressure of 150 MPa also show a semi-circle, but with a lower resistance of  $\sim 20 \Omega$ . If a pressure of 400 MPa is applied, the semi-circle vanishes to a negligible size, indicating that it originates from electronic resistances which decrease upon compression. These might be caused by inter-particle electronic resistances within the electrodes and/or by a contact resistance between the current collector/electrode interface. Trying to distinguish between these two electronic resistance contributions, it is noteworthy that these additional semi-circles were only observed for electrodes coated on aluminum foil, but were never observed for graphite or LTO electrodes coated on copper foil. Considering that the intrinsic electronic conductivity of LTO ( $10^{-13} \text{ S/cm}^{46}$ ) is lower than that of LFP ( $10^{-9} \text{ S/cm}^{47}$ ) and considering that the LFP electrodes shown in Figure 12 were prepared with a high conductive carbon content (15%wt), the origin of the semi-circle in Figure 12 is most probably related to an electronic contact resistance between the current collector/coating interface rather than to inter-particle resistances within the electrode. This is further supported by estimating the effective capacitance of the semi-circle feature in Figure 12, obtained from its frequency at the semi-circle apex and its corresponding resistance, which amounts to  $1 \mu\text{F}$ : at an approximate double layer capacitance of on the order of  $10 \mu\text{F/cm}^2$ , this would equate to an effective interfacial area of about  $0.1 \text{ cm}^2$ , which is four orders of magnitude smaller than the electrode material surface area ( $\sim 980 \text{ cm}^2$  based on  $2.58 \text{ mg}_{\text{LFP}}/\text{cm}^2$  at  $24 \text{ m}^2/\text{g}$  BET area and  $0.58 \text{ mg}_{\text{carbon}}/\text{cm}^2$  at  $62 \text{ m}^2/\text{g}$  BET area).

The results and conclusions drawn here are in accordance with the work by Gaberscek et al.,<sup>48</sup> who argued that the semi-circle results from a parallel connection of the current collector/coating contact resistance and the current collector's double layer capacitance. Analogous to Figure 12, they also observed a reduced semi-circle resistance upon applying external pressure, whereby the magnitude of resistance change upon compression reported by Gaberscek et al. correlates well with our findings; in addition, they also showed a pronounced decrease of the contact resistance when copper instead of aluminum foil is used as a current collector. Current collector/coating contact resistances were also quantified by Illig<sup>49</sup> by analyzing the distribution of relaxation times of impedance spectra obtained with symmetrical cells.

In summary, our above measurements using a non-intercalating salt to realize a true blocking electrode configuration allow for a precise and unambiguous determination of potentially present contact resistances, without the interference from charge transfer reactions. In addition, as long as a transmission-line behavior can be observed, the ionic resistance through the electrode can still be determined, despite the serial addition of a contact resistance element ( $R_C/Q_{\text{DBL}}$ ). From the results shown in Figure 12, it is apparent that a crucial step particularly during cathode electrode manufacturing is the reduction of the aluminum current collector/coating contact resistance by electrode compression/calendering. Measurements in symmetrical cells with a non-intercalating electrolyte as presented above offer a quick and reliable method to characterize the contact resistance of electrodes after the manufacturing process.

**Reproducibility and validation.**—In the following, the validity and reproducibility of the TLM-Q approach to determine the ionic resistance of electrodes will be demonstrated by varying electrolyte conductivity and electrode area. For this, impedance measurements in symmetrical pouch cells and T-Cells with graphite electrodes (graphite-1, see Table I) were done using an electrolyte containing 10, 50, 200, and 700 mM TBAClO<sub>4</sub> in EC:DMC (1:1 w:w).

Figure 13 shows the impedance spectra of symmetric graphite pouch cells (graphite-1, see Table I) and their excellent agreement with Eq. 11. As expected, the HFR increases together with the ionic

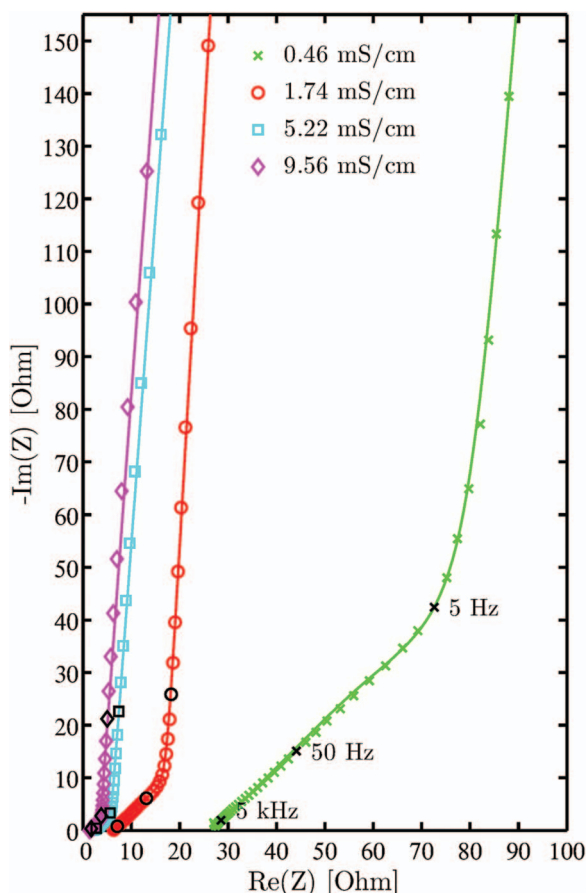


**Figure 13.** Impedance spectra and fits with Eq. 11 of four symmetrical graphite pouch cells (graphite-1 electrodes with  $\varepsilon = 0.42 \pm 0.02$ , see Table I) with EC:DMC (1:1 w:w) containing 10, 50, 200, and 700 mM TBAClO<sub>4</sub> (electrolyte conductivities  $\kappa$  are listed in the figure). Impedance data were recorded between 200 kHz and 0.5 Hz; the 5 kHz, 50 Hz, and 5 Hz data are indicated by the black symbols.

resistance ( $R_{\text{ion}}$ ) in the electrode when the electrolyte conductivity ( $\kappa$ ) is decreased. The observed constant phase angle  $\gamma$  was found to be similar for each type of active material. In the case of graphite (compare Figure 13), constant phase angles in the low frequency range of 85° were found. For other active materials we found values ranging from 88° (LTO) to 80° (LFP). Due to the systematic correlation with the type of active material, we ascribe the constant phase behavior to the type and structure of the electrode surfaces.<sup>41</sup> After quantification of  $R_{\text{ion}}$  from the impedance data, the tortuosity of the electrodes can be obtained by rearranging Eq. 8,

$$\tau = \frac{R_{\text{ion}} A \kappa \varepsilon}{2 d} \quad [13]$$

where the porosity  $\varepsilon$  of the electrodes can be determined from the areal weight and the thickness of the electrodes (see Experimental section); the factor 2 accounts for the symmetry of the setup, where the sum of the impedances of two identical electrodes is measured.

To compare the possible influence of electrolyte conductivity and cell setup, the tortuosities calculated from Eq. 13 based on impedance measurements with symmetrical graphite electrodes (graphite-1, see Table I) from eight T-Cells (two for each salt concentration) and the four pouch cells shown in Figure 13 are plotted vs. electrolyte conductivity in Figure 14. For these graphite electrodes with a porosity of  $\varepsilon = 0.43 \pm 0.02$ , an average tortuosity of  $\tau = 4.3 \pm 0.6$  is obtained, which is ~3-fold higher than the value of  $\tau = 1.5$  which would be predicted by the Bruggeman equation for spherical particles with  $\alpha = 0.5$  (Eq. 6), which is used quite frequently in battery models. It is emphasized

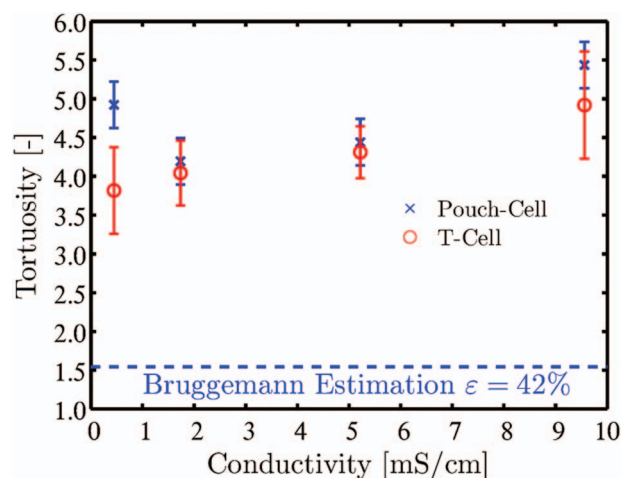


**Figure 14.** Influence of electrolyte conductivity on the determined tortuosities in symmetrical pouch and T-Cells with graphite electrodes (graphite-1, see Table I, with  $d_{\text{Coating}} = 58 \pm 2 \mu\text{m}$ ,  $\varepsilon \approx 0.43 \pm 0.02$ ) using four different electrolytes, viz., EC:DMC (1:1 w:w) with 10, 50, 200, and 700 mM TBAClO<sub>4</sub> (see Figure 13 for electrolyte conductivity values). The Bruggeman estimation for spherical particles with  $\alpha = 0.5$  is represented by the dashed horizontal line. Error bars indicate the standard deviation of two T-Cells per electrolyte or a constant error of 0.3 for the pouch cells, which was estimated using the Gaussian variance with experimental deviations of effective area, electrolyte conductivity and determined electrode thickness and porosity.

that not all electrodes are 100% identical and a certain variance results from the laboratory scale electrode preparation process. Nonetheless, Figure 14 shows a reasonably good agreement between T-Cells and pouch cells with very different electrode areas and over a large range of electrolyte conductivities. In the following experiments with different electrodes, compressed to different porosities, we have chosen a TBAClO<sub>4</sub> concentration of 10 mM, which results in a tortuosity of  $\tau = 4.2 \pm 0.7$  for the graphite electrodes shown in Figure 13. A 10 mM concentration was chosen to best fulfill the requirements for the simplification of the transmission line model (see Figure 3), i.e., negligible electronic resistance in the electrode compared to the ionic resistance inside the electrolyte. It should be noted that in comparison to the tortuosity determination of separators, small but finite contact resistances do not affect the determination of electrode tortuosities.

**Drivers of the tortuosity of porous electrodes.**—In this Section, we will investigate the effect of particle morphology, particle size, and electrode composition on the ionic resistance of porous electrodes. Where possible, the data will be compared to the literature. As typical electrode porosities in lithium ion batteries are adjusted to roughly 30% by calendering/compression of electrodes, we will first focus on electrodes prepared from different active materials which were compressed to porosities near 30% and which have an active material content of  $\geq 90\%$ wt (see Table I).

The MacMullin numbers for electrodes with different active materials shown in Figure 15 are calculated based on the ionic resistances obtained from the difference between the extrapolated x-axis intercepts of the low and the medium frequency regions in the impedance spectra as explained above (see Figure 11). Horizontal error bars indicate the uncertainty in the porosity (see Experimental section), while vertical error bars are based on the error on the thickness measurement ( $d$ ), which affects the calculation of the MacMullin number calculated from a combination of Eqs. 5 and 13 (note that  $N_M$  thus is independent of  $\varepsilon$ ). MacMullin numbers around 18-19 are obtained for the two examined graphite electrodes at porosities of ~29% (graphite-1) and ~35% (graphite-2). At a similar porosity, NMC electrodes have an almost 2-fold lower MacMullin number of 10-11. This difference is ascribed to the difference in particle morphology, which is illustrated by comparative top-view and cross-sectional-view scanning electron



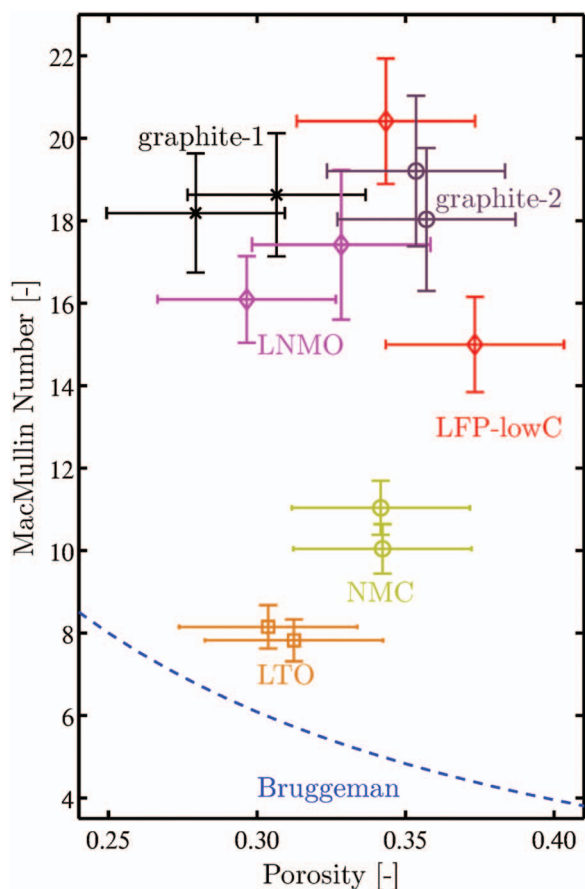


**Figure 15.** MacMullin numbers of electrodes with active material contents  $\geq 90\%$  as specified in Table 1 and compressed to porosities ranging between 0.27 and 0.37. Results are obtained from measurements in pouch cells and T-Cells using EC:DMC (1:1 w:w) with 10 mM TBAClO<sub>4</sub> as an electrolyte. The Bruggeman prediction for spherical particles ( $\alpha = 0.5$ ,  $N_{M(B)} = \varepsilon^{-1.5}$ ) is indicated by the blue dashed line.

microscope (SEM) images shown in Figure 16. Both active materials have large particles in the range of 10–30  $\mu\text{m}$ , but while NMC particles are quite spherical, graphite particles have a plate-like morphology elongated in two directions. Since in the electrode coating process, graphite particles align preferentially horizontally (see Figure 16), it can be imagined easily, that ionic conduction will be hindered to a larger extent by the horizontally aligned graphite particles compared to spherical particles. This effect was also described by numerical evaluations of the tortuosity of graphite electrodes based on FIB-SEM derived morphologies, yielding  $\sim 2$ -fold higher through-plane compared to in-plane tortuosities.<sup>16</sup> Similarly, two independent numerical evaluations of the tortuosity of spherical (like NMC) vs. plate-like particles (like graphite), yielded much higher values for the latter.<sup>2,32</sup> Thus, all three numerical evaluations are at least qualitatively consistent with the substantially lower tortuosities for NMC compared to graphite electrodes shown in Figure 15. Quantitatively, however, the numerical investigations based on 3D reconstructed geometries deviate substantially from our experimental results. For example, the analysis of 3D reconstructed electrodes of spherical NMC particles by Ebner et al.<sup>32</sup> yields through-plane tortuosity values very close to the Bruggeman equation for spherical particles ( $\tau = \varepsilon^{-0.5}$ ) while our experimentally obtained values are two-fold larger than the latter prediction (see Figure 15). One reasonable explanation for this discrepancy can be the limited resolution of the used imaging technique, which will at best only partly resolve the conductive carbon and binder morphology, eventually assuming more empty pores than actually exist. In addition, the authors themselves state that their findings “are based on purely geometrical arguments”<sup>32</sup> which due to the different definitions of the tortuosity (geometrically, mathematically or physically; see very first section of this paper) may lead to different values compared to our electrochemical AC impedance spectroscopy measurements.

The influence of particle size can be demonstrated by comparing the MacMullin numbers of LNMO and LTO electrodes (composition see Table 1), for which values of  $\sim 17$  and  $\sim 8$  are found, respectively (see Figure 15). Both active materials have a rather spherical morphology but the difference in particle size is obvious from Figure 17. LTO particles have a spherical/cube-like morphology with a size of about 1–2  $\mu\text{m}$ , whereas LNMO particles have a particle size around 10–20  $\mu\text{m}$ . We hypothesize that the observed difference in effective ionic transport resistance can be explained with a partial blockage of

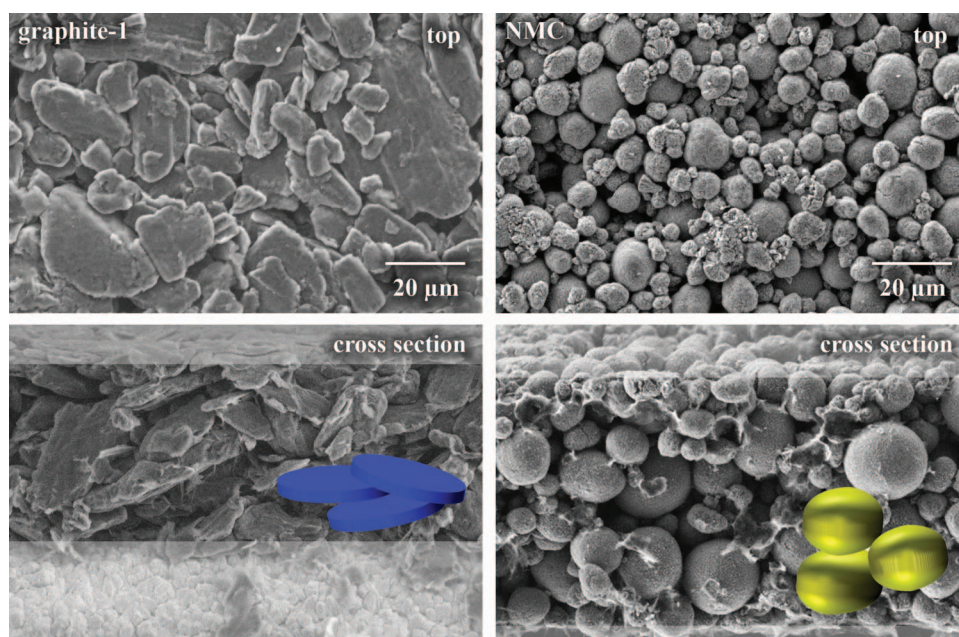


**Figure 16.** SEM top-view (upper figures) and cross-sectional-view (lower figures) micrographs of graphite-1 ( $\varepsilon \approx 0.29$ ) and NMC ( $\varepsilon \approx 0.34$ ) electrodes (composition see Table 1), with a schematic representation of the particle morphology. The scale bar applies for both the top-views and the cross-sections.



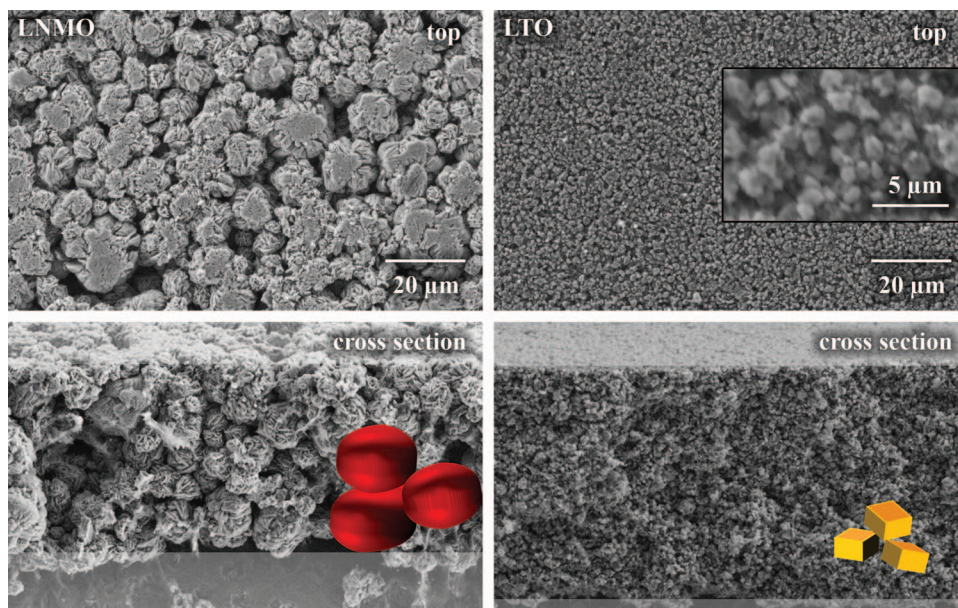


**Figure 17.** SEM top view and cross section micrographs of LNMO ( $\epsilon \approx 0.31$ ) and LTO ( $\epsilon \approx 0.30$ ) electrodes (composition see Table I), with schematic representation of particle morphology. The scale bar applies for both the top-views and the cross-sections.

the pores. Detours around a blocked pore are longer for large LNMO particles compared to small LTO particles.

The aforementioned effect of the particle size on the electrode tortuosity can also be observed if electrodes with the same active material but with different conductive carbon content are compared. This is seen best by examining their MacMullin numbers over a wider range of porosity, i.e., from  $\sim 25\%$  to  $\sim 75\%$ , which also allows to evaluate the functional relationship between tortuosity and porosity using Eq. 7. Figure 19 thus compares the MacMullin numbers of LFP electrodes with either low or high carbon content (LFP-lowC and LFP-highC see Table I) versus porosity. To understand the impact of the conductive additive on the electrodes' microstructure, we first have to compare the morphologies of the LFP active material and the conductive carbon. The conductive carbon used in this work, consists of very small primary particles ( $\sim 40$  nm diameter) which are fused together in branch-like structures of several hundreds of nm in length. On the other hand, the LFP active material consists of 4 to  $20 \mu\text{m}$  sized weak agglomerates (see Figure 18) of primary LFP particles of  $< 500$  nm size.

Viewing the surface of the compressed LFP electrodes shown in Figure 18, broken LFP agglomerates can be easily spotted. Quite obviously, higher amounts of conductive carbon lead to a more effective separation of the LFP primary agglomerates, providing shorter ionic pathways into the center of the LFP agglomerates. In other words, we believe that owing to their high hardness, the conductive carbons function as incompressible scaffolds between the more compressible primary agglomerates of the LFP, which allows for a faster ionic transport.

As expected, the MacMullin numbers increase with decreasing  $\epsilon$ , as shown in Figure 19, an effect which can be described by a fit of the data to a combination of Eqs. 5 and 7. To deconvolute the effect of porosity decrease and tortuosity change, MacMullin numbers of Figure 19 are multiplied with the porosity to obtain the tortuosity values depicted in Figure 20.

As tortuosities are calculated from MacMullin numbers using the experimentally determined porosities (see Experimental section), the y-errors increase compared to Figure 19. Also shown in Figure 19 and Figure 20 are fits of the experimentally obtained MacMullin numbers

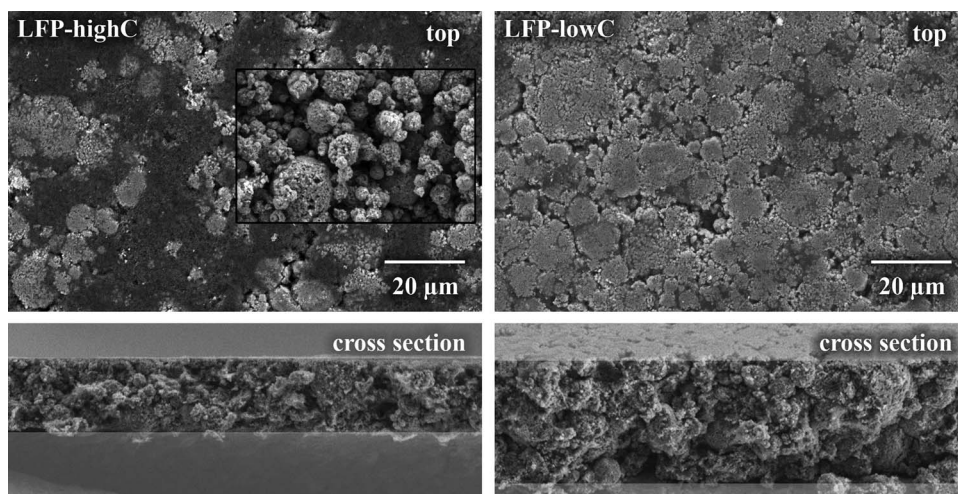


**Figure 18.** SEM top-view and cross-sectional-view of LFP-highC ( $\epsilon \approx 0.27$ ) and LFP-lowC ( $\epsilon \approx 0.27$ ) electrodes specified in Table I. Inset of LFP-highC depicts active material powder. The scale bar applies for both the top-views and the cross-sectional-views.

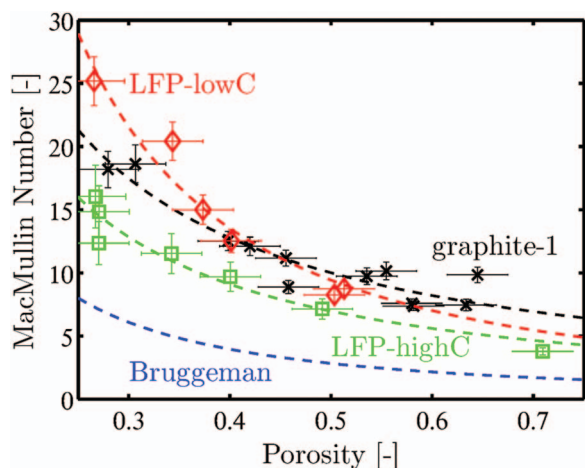


**Figure 19.** MacMullin numbers of LFP electrodes with an active material content of 70% (LFP-highC, see Table I) or 90% (LFP-lowC, see Table I) as well as of graphite electrodes (graphite-1, see Table I). Results are obtained from measurements in pouch cells and T-Cells using EC:DMC (1:1 w:w) with 10 mM TBAClO<sub>4</sub> as electrolyte. Data are fitted with a combination of Eq. 5 and Eq. 7:  $N_M = 4.7 \varepsilon^{-1.1}$  (graphite-1),  $N_M = 3.1 \varepsilon^{-1.6}$  (LFP-lowC), and  $N_M = 3.0 \varepsilon^{-1.2}$  (LFP-highC). The Bruggeman prediction for spherical particles ( $\alpha = 0.5$ ,  $N_{M(B)} = \varepsilon^{-1.5}$ ) is indicated by the blue dashed line.

and tortuosities with the generalized Bruggeman equation (Eq. 7). For all types of electrodes shown in these figures, the experimental data of  $N_M$  or  $\tau$  vs.  $\varepsilon$  could only be properly represented when a variable prefactor  $f$  was used in the fits. We would like to emphasize that the experimental data could not be represented by a generalized Bruggeman equation with the prefactor  $f = 1$ , contrary to what was reported in studies with 3D reconstructed electrodes.<sup>32</sup> Comparison of the two plots show that the porosity dependence of the MacMullin number is mainly due to the decrease in available electrolyte pore volume, i.e., a decrease of the porosity. Tortuosities of graphite-1 and LFP electrodes with high conductive carbon content (LFP-highC) only show a small porosity dependence within the error bars, increasing from  $\sim 4.8$  to  $\sim 5.2$  and from  $\sim 3.5$  to  $\sim 4.2$ , respectively, as the porosity decreases from  $\sim 70$  to  $\sim 30\%$ . While LFP electrodes with 5%wt conductive carbon (LFP-lowC) have a similar tortuosity as those with 15%wt conductive carbon (LFP-highC) at high porosity, the former

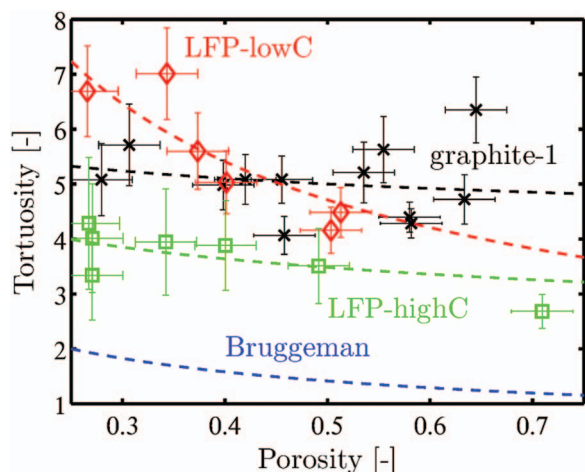


**Figure 20.** Tortuosities of LFP electrodes with 70% or 90% active material and graphite electrodes at different compositions and porosities. Results are obtained from measurements in pouch cells and T-Cells using EC:DMC (1:1 w:w) with 10 mM TBAClO<sub>4</sub> as electrolyte. Dashed lines are based on the fitting results from Figure 19:  $\tau = 4.7 \varepsilon^{-0.1}$  (graphite-1),  $\tau = 3.1 \varepsilon^{-0.6}$  (LFP-lowC),  $\tau = 3.0 \varepsilon^{-0.2}$  (LFP-highC). The Bruggeman prediction for spherical particles ( $\alpha = 0.5$ ,  $\tau = \varepsilon^{-0.5}$ ) is indicated by the blue dashed line.

show a steep increase in tortuosity from  $\sim 4.5$  at 50% porosity to  $\sim 7$  at 30%. Comparison with the SEM micrographs given in Figure 18 shows, that the primary agglomerates of the LFP are broken at the higher compressive forces required to obtain low porosities. At least at the surface of these electrodes, this leads to a plate-like particle shape, from which an increase in ionic resistance is expected as argued before. As suggested by viewing Figure 18, the lateral dimensions of these compression induced plate-like particles is larger at lower conductive carbon content, so that the effect of primary agglomerate deformation of the LFP on the tortuosity and the MacMullin number is more pronounced at lower conductive carbon content.

Tortuosities of graphite electrodes (graphite-1) in Figure 20 show no dependence on the porosity. In our opinion, the open pores between the horizontally aligned graphite particles are unaltered upon electrode compression normal to the current collector plane so that the observed change in porosity has to be ascribed to a compression of the soft graphite particles. In stark contrast to our experimentally determined tortuosities of platelet-shaped graphite particles, very different results are obtained from an analysis of 3D reconstructed graphite electrodes.<sup>32</sup> While the reported tortuosity of  $\sim 5.5$  at a porosity of 0.4 is in agreement with our experimental results, the reported tortuosity of 3 for an electrode porosity of 0.6 is very different from our data (see Figure 20). As argued above, the discrepancy may result from the inability to sufficiently resolve binder and carbon particles in the 3D reconstructed electrodes as well as from the purely geometrical nature of analysis of the tortuosity in the publication.<sup>32</sup> Additionally, as shown by our findings and also by the geometrical analysis of the influence of particle anisotropy on the electrode tortuosity,<sup>32</sup> a direct comparison might only be valid for electrodes of identical composition and, more importantly, the same particle size and shape.

**Literature comparison.**—From the above discussion, it is clear that the porosity dependence of the effective tortuosities and MacMullin numbers of porous electrodes even made of the same active material strongly depend on the amount and most likely the type of conductive carbon, which must be kept in mind when comparing  $\tau$  and  $N_M$  values with the literature. Figure 21 depicts a comparison of the MacMullin numbers vs. porosity obtained in this work for LFP electrodes with those reported in the literature. Also shown in Figure 21 is the Bruggeman relation for spherical particles  $N_{M(B)} = \varepsilon^{-1.5}$ , which is frequently used in battery models.

The comparison in Figure 21 shows MacMullin numbers ranging from  $\sim 3$ –7 for electrodes at a porosity of 60–70%, in the porosity range of commercially used electrodes ( $\sim 30$ –35%), the reported MacMullin numbers increase to  $\sim 7$ –20. The mismatch between the Bruggeman equation for spherical particles ( $\alpha = 0.5$ , dashed blue line in Figure 21) and the MacMullin numbers shown in Figure 21 (compare also Figure 15) is  $\sim 1.5$  to  $\sim 3$ -fold, particularly at low porosities, an observation which has been made before.<sup>18,21,29</sup> For example, higher ionic resistances than suggested by the Bruggemann equation are reported by Thorat et al.<sup>18</sup> (brown line in Figure 21), who use Eq. 7 to fit tortuosities obtained from fits of polarization-interrupt experiments. Cooper et al.<sup>12</sup> used a synchrotron X-ray tomography to reconstruct a commercial LFP electrode and obtained MacMullin numbers between 6 and 10 from heat transport simulations (orange circles). In Ender et al.,<sup>34</sup> electrode morphology reconstruction using a FIB-SEM and subsequent solution of the Laplace equation was done for lab-scale LFP electrodes with a particle size of  $\sim 100$  nm and with commercially prepared LFP electrodes with a secondary agglomerate LFP particle size of  $\sim 1.2 \mu\text{m}$ , obtaining MacMullin numbers of  $\sim 2.5$  and  $\sim 5$  respectively (green diamonds). In contrast to these reports on LFP based electrodes, somewhat higher MacMullin numbers are obtained in our study for the LFP electrodes with high conductive carbon content (LFP-highC, see green line in Figure 21), but the functional relationship between  $N_M$  and  $\varepsilon$  follows a similar trend. Unfortunately, owing to the strong dependence of active material morphology (see Figure 15) and conductive carbon content (see Figure 19), a rigorous comparison between the  $N_M$  values obtained by the methodologies used here and in the literature is not possible.



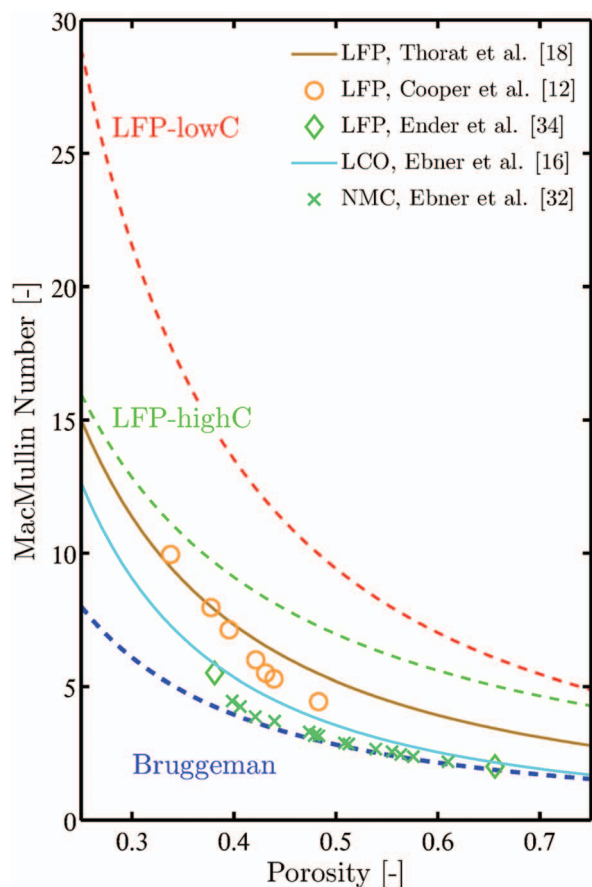


**Figure 21.** Comparison of the MacMullin numbers vs. porosity for the LFP electrodes studied in this work (LFP-lowC with 90/5/5 AM/binder/C and LFP-highC with 70/15/15 AM/binder/C, taken from Figure 19) with literature values from Thorat et al.<sup>18</sup> (LFP with 84/8/8 AM/binder/C, potato shaped, 300–600 nm length), Cooper et al.<sup>12</sup> (LFP, electrode composition unknown), Ender et al.<sup>34</sup> (LFP with 70/6/24 AM/binder/C, potato shaped, 200–600 nm length), Ebner and Wood<sup>16</sup> (LCO with ~94/3/3 AM/binder/C, non-spherical, 10  $\mu\text{m}$ ) and Ebner et al.<sup>32</sup> (NMC with 96/2/2 AM/binder/C, spherical, 20  $\mu\text{m}$ ). The Bruggeman prediction for spherical particles ( $\alpha = 0.5$ ,  $N_{\text{M(B)}} = \varepsilon^{-1.5}$ ) is indicated by the blue dashed line.

Even though different active materials may result in very different MacMullin numbers (see Figure 15), we have added data on LCO and NMC electrodes in Figure 21, which were reported by Ebner and Wood<sup>16</sup> and Ebner et al.,<sup>32</sup> who developed a software called *Bruggeman Estimator* to obtain the tortuosity of porous electrodes from top and cross section SEM micrographs. The close relation of the MacMullin numbers of these NMC electrodes with the Bruggeman equation have been discussed critically above. For a LCO cathode, they report a Bruggeman exponent for the through plane tortuosity of  $\alpha = 0.83$  (i.e.,  $\tau = \varepsilon^{-0.83}$ ), from which we calculated the MacMullin number data shown in Figure 21 (cyan line). The functional relationship between  $N_{\text{M}}$  and  $\varepsilon$  is again very similar to that observed for the literature data and for the LFP-highC data in Figure 21, whereby it is noteworthy that the conductive carbon content in the LCO electrodes is only 3%wt, which in the case of our LFP electrodes (LFP-lowC, see red line in Figure 21) yields ~2-fold higher  $N_{\text{M}}$  values.

### Conclusions

MacMullin numbers as well as tortuosities of commonly used lithium ion battery separators measured in a custom made copper block setup are listed in the present study. The standard deviations for these measurements were shown to be below 8%. Our new measurement procedure was validated by systematic variation of experimental

parameters like cell type, electrolyte conductivity, and number of separator layers.

We also showed an impedance based approach to quantify the ionic resistance in lithium ion battery electrodes, from which electrode tortuosities and MacMullin numbers can be determined. This method uses a simple transmission-line model in a blocking configuration, which is achieved by employing a non-intercalating electrolyte salt. We showed that an increased accuracy can be obtained when using constant-phase elements rather than ideal capacitors, as previously done in the literature. The invariance of the measured tortuosities with respect to electrolyte conductivity and electrode area was verified. Additionally while composite electrodes coated on copper current collectors always exhibited a perfect transmission-line model behavior, a distinct high frequency semi-circle was found for some LFP electrodes coated on aluminum current collector. In accordance with the literature, this semi-circle could be identified as a contact resistance between aluminum and the electrode coating, which was possible due to the absence of charge transfer reactions when using a non-intercalating electrolyte.

For all types of investigated electrodes, the MacMullin numbers are found to be ~1.5–3 times larger than suggested by the Bruggeman equation for spherical particles ( $\alpha = 0.5$ ), which is frequently used in battery models. Furthermore, we showed the strong impact of active material particle size / morphology and conductive carbon content on the ionic conduction resistance.

### Acknowledgment

We thank Daniel Pitzl and Simon Abendschein from our group for preparation of some of the electrodes. J. L. and A.E. gratefully acknowledge the funding by the Bavarian Ministry of Economic Affairs and Media, Energy, and Technology for its financial support under the auspices of the EEBatt project. Funding for J. H. was provided by the BMBF (Federal ministry of Education and research, Germany), ExZellTUM project, grant number 03X4633A. The authors thank SI Analytics for manufacturing the used custom made conductivity sensors.

**Note added in proof.**—A detailed discussion of the origin and the application of the Bruggeman relation in battery electrodes can also be found in Ref. 50.

### List of Symbols

Symbol	Name	Unit
$N_{\text{M}}$	MacMullin number	-
$\kappa$	electrolyte conductivity	mS/cm
$\kappa_{\text{eff}}$	effective electrolyte conductivity in porous medium	mS/cm
$\varepsilon$	porosity of porous medium	-
$m$	Archie's exponent	-
$\tau$	tortuosity of porous medium	-
$\alpha$	Bruggeman exponent	-
$f$	proportionality factor	-
$d$	length	$\mu\text{m}$
$\beta$	constriction factor	-
$R$	resistance	$\Omega$
$A$	area	$\text{cm}^2$
$Z$	complex impedance	$\Omega$
$Q$	constant-phase capacitance	$\text{F s}^{\gamma-1}$
$i$	imaginary unit	-
$\omega$	angular frequency	1/s
$\gamma$	constant phase exponent	-
$r$	resistances*	$\Omega$
$q$	constant phase capacitance*	$\text{F s}^{\gamma-1}$
$z$	complex impedance*	$\Omega$

\*in a differential segment of the electrode/electrolyte.



## References

1. J. Newman and K. Thomas-Alyea, *Electrochemical Systems*, 3rd ed., Wiley Interscience, Hoboken, (2004).
2. K. K. Patel, J. M. Paulsen, and J. Desilvestro, *J. Power Sources*, **122**, 144 (2003).
3. G. E. Archie, *Pet. Technol.*, 54 (1942).
4. L. Shen and Z. Chen, *Chem. Eng. Sci.*, **62**, 3748 (2007).
5. M. Barrande, R. Bouchet, and R. Denoyel, *Anal. Chem.*, **79**, 9115 (2007).
6. L. Holzer, D. Wiedenmann, B. Münch, L. Keller, M. Prestat, P. Gasser, I. Robertson, and B. Grobty, *J. Mater. Sci.*, **48**, 2934 (2013).
7. M. R. J. Wyllie and W. Rose, *J. Pet. Technol.*, **2**, 105 (1950).
8. D. Cornell and D. L. Katz, *Ind. Eng. Chem.*, **45**, 2145 (1953).
9. J. M. Zalc, S. C. Reyes, and E. Iglesia, *Chem. Eng. Sci.*, **59**, 2947 (2004).
10. D. Wiedenmann, L. Keller, L. Holzer, J. Stojadinović, B. Münch, L. Suarez, B. Fumey, H. Hagendorfer, R. Brönnimann, P. Modregger, M. Gorbar, U. F. Vogt, A. Züttel, F. La Mantia, R. Wepf, and B. Grobty, *AIChE J.*, **59**, 1446 (2013).
11. F. Tariq, V. Yufit, M. Kishimoto, P. R. Shearing, S. Menkin, D. Golodnitsky, J. Gelb, E. Peled, and N. P. Brandon, *J. Power Sources*, **248**, 1014 (2014).
12. S. J. Cooper, D. S. Eastwood, J. Gelb, G. Damblanc, D. J. L. Brett, R. S. Bradley, P. J. Withers, P. D. Lee, P. D. A., J. Marquis, N. P. Brandon, and P. R. Shearing, *J. Power Sources*, **247**, 1033 (2014).
13. M. B. Clennell, *Geol. Soc. London, Spec. Publ.*, **122**, 299 (1997).
14. D. Djian, F. Alloin, S. Martinet, H. Lignier, and J. Y. Sanchez, *J. Power Sources*, **172**, 416 (2007).
15. J. Joos, T. Carraro, A. Weber, and E. Ivers-Tiffée, *J. Power Sources*, **196**, 7302 (2011).
16. M. Ebner and V. Wood, *J. Electrochem. Soc.*, **162**, A3064 (2014).
17. D. A. G. Bruggeman, *Ann. Phys.*, **24**, 636 (1935).
18. I. V. Thorat, D. E. Stephenson, N. A. Zacharias, K. Zaghib, J. N. Harb, and D. R. Wheeler, *J. Power Sources*, **188**, 592 (2009).
19. R. E. De La Rue and C. W. Tobias, *J. Electrochem. Soc.*, **109**, 827 (1959).
20. R. B. Macmullin and G. A. Muccini, *AIChE J.*, **2**, 393 (1956).
21. D.-W. Chung, M. Ebner, D. R. Ely, V. Wood, and R. Edwin García, *Model. Simul. Mater. Sci. Eng.*, **21**, 074009 (2013).
22. K. M. Abraham, *Electrochim. Acta*, **38**, 1233 (1993).
23. P. Arora and Z. J. Zhang, *Chem. Rev.*, **104**, 4419 (2004).
24. V. F. Lvovich, *Impedance Spectroscopy Applications to Electrochemical and Dielectric Phenomena*, p. 356, John Wiley & Sons, Ltd, New Jersey, (2012).
25. Y. Liu, M. W. Murphy, D. R. Baker, W. Gu, C. Ji, J. Jorne, and H. A. Gasteiger, *J. Electrochem. Soc.*, **156**, B970 (2009).
26. N. Ogihara, S. Kawauchi, C. Okuda, Y. Itou, Y. Takeuchi, and Y. Ukyo, *J. Electrochem. Soc.*, **159**, A1034 (2012).
27. N. Ogihara, Y. Itou, T. Sasaki, and Y. Takeuchi, *J. Phys. Chem. C*, 150209102507001 (2015).
28. N. A. Zacharias, D. R. Nevers, C. Skelton, K. Knackstedt, D. E. Stephenson, and D. R. Wheeler, *J. Electrochem. Soc.*, **160**, A306 (2013).
29. T. DuBeshter, P. K. Sinha, A. Sakars, G. W. Fly, and J. Jorne, *J. Electrochem. Soc.*, **161**, A599 (2014).
30. M. Ebner, F. Geldmacher, F. Marone, M. Stamparoni, and V. Wood, *Adv. Energy Mater.*, **3**, 845 (2013).
31. S. J. Harris and P. Lu, *J. Phys. Chem. C*, **117**, 6481 (2013).
32. M. Ebner, D. W. Chung, R. E. García, and V. Wood, *Adv. Energy Mater.*, **4**, 1 (2014).
33. L. Zielke, T. Hutzenlaub, D. R. Wheeler, I. Manke, T. Arlt, N. Paust, R. Zengerle, and S. Thiele, *Adv. Energy Mater.*, **4**, 1 (2014).
34. M. Ender, J. Joos, T. Carraro, and E. Ivers-Tiffée, *J. Electrochem. Soc.*, **159**, A972 (2012).
35. M. Ender, J. Joos, T. Carraro, and E. Ivers-Tiffée, *Electrochem. commun.*, **13**, 166 (2011).
36. Andrzej Lasia, *Electrochemical Impedance Spectroscopy and its Applications*, p. 1-117 (2004).
37. C. H. Kim, S. I. Pyun, and J. H. Kim, *Electrochim. Acta*, **48**, 3455 (2003).
38. J.-B. Jorcin, M. E. Orazem, N. Pébère, and B. Tribollet, *Electrochim. Acta*, **51**, 1473 (2006).
39. M. Ender, A. Weber, and E. Ivers-Tiffée, *Electrochem. commun.*, **34**, 130 (2013).
40. C.-W. C. Wang, A. M. Sastry, K. A. Striebel, K. Zaghib, and A. Marie, *J. Electrochem. Soc.*, **152**, A1001 (2005).
41. W. H. Mulder, J. H. Sluyters, T. Pajkossy, and L. Nyikos, *J. Electroanal. Chem. Interfacial Electrochem.*, **285**, 103 (1990).
42. M. Eikerling and A. A. Kornyshev, *J. Electroanal. Chem.*, **475**, 107 (1999).
43. Freudenberg, *Prod. Specif. Sheet* (2015).
44. J. Cannarella and C. B. Arnold, *J. Power Sources*, **226**, 149 (2013).
45. Celgard, *Prod. Specif. Sheet* (2014).
46. C. H. Chen, J. T. Vaughey, A. N. Jansen, D. W. Dees, A. J. Kahaian, T. Goacher, and M. M. Thackeray, *J. Electrochem. Soc.*, **148**, A102 (2001).
47. K. Zaghib, A. Mauger, J. B. Goodenough, F. Gendron, and C. M. Julien, *Chem. Mater.*, **19**, 3740 (2007).
48. M. Gaberscek, J. Moskon, B. Erjavec, R. Dominko, and J. Jamnik, *Electrochem. Solid-State Lett.*, **11**, A170 (2008).
49. J. N. Illig, PhD Thesis, Karlsruhe (2014).
50. B. Tjaden, S. J. Cooper, D. J. L. Brett, and D. Kramer, *Nanotechnology, Sep. Eng.*, **12**, 44 (2016).